Vortex dynamics in a shearing zonal flow

By PHILIP S. MARCUS

Department of Mechanical Engineering, University of California at Berkeley,
Berkeley, CA 94720, USA

When vortices are embedded in a shearing zonal flow their interactions are changed qualitatively. If the zonal flow's shear and the vortex's strength are of the same order and opposite sign, the vortex is pulled into a thin spiral, fragments, and is destroyed in a turn-around time. If the signs are the same, the vortex redistributes its vorticity so that its maximum value is at the centre, and its shape is determined by the ratio of its vorticity to the shear of the surrounding zonal flow. The dynamics depends crucially on the exchange between the self-energy of the vortices and the interaction energy of the zonal flow with the vortices. A numerical example that shows all of these effects is the breakup of a vortex layer: either a single large vortex is formed or successively smaller and more numerous thin filaments of vorticity are created. Two stable vortices are shown to merge if their initial separation in the cross-zonal direction is smaller than a critical distance which is approximately equal the vortices' radii. The motions of large vortices are constrained by conservation laws, but when the zonal flow is filled with small-scale filaments of vorticity, the large vortices exchange energy with the filaments so that they are no longer constrained by these laws, and their dynamics become richer. Energy is shown to flow from the large vortices to the filaments, and this observation is used to predict the strength of boundary layers and the critical separation distance for vortex merging.

1. Introduction

Large vortices are interesting because of their longevity, their robustness to large perturbations, their coexistence with surrounding turbulence, and their ubiquity in laboratory, geophysical, and astrophysical flows. There have been numerous studies of the stability, interactions, and mergers of small numbers of isolated monopolar and dipolar vortices (cf. Overman & Zabusky 1982; Flierl, Stern & Whitehead 1983; Melander, Styczek & Zabusky 1984; Buttke 1990). In this paper we extend the study of two-dimensional vortices by examining their behaviour when they are embedded in shearing zonal flows. Our study is motivated by the fact that vortices frequently appear in zonal flows and by our observation that zonal flows greatly alter vortex interactions. Examples of zonal flows containing vortices are laboratory mixing layers, the Gulf Stream, and the East–West winds of Jupiter, Saturn, and Neptune.

The addition of a zonal flow complicates the vortex dynamics not only because the zonal flow advects and shears the vortices, but also because the vortices react back upon and change the zonal flow. Disentangling the physics of all of these processes from a numerical simulation or an experiment can be extremely difficult, so this study is restricted to zonal flows with uniform and approximately uniform potential vorticity ω_p. (As we show in §2 of this paper, this class of zonal flows is very broad, and in fact *any* zonal flow can be made to have uniform potential vorticity if the

bottom boundary condition is chosen properly.) The advantage of studying a zonal flow with uniform potential vorticity is that the zonal flow affects the vortices, but the vortices do not affect the zonal flow (Marcus 1986, 1987). Hence, the zonal velocities are approximately constant during the vortex interactions, and the vortex dynamics are simpler to understand. We have found that when the zonal flows do not have uniform ω_p, the zonal velocities evolve with the same timescale as the vortices. Although this is no more difficult to compute, a physical interpretation of the dynamics is more difficult. A second motivation for studying vortices in zonal flows with uniform ω_p is that these zonal flows occur frequently because one of the ways in which vortices react back upon a zonal flow is by making its potential vorticity homogeneous (Rhines & Young 1982). For example, Nielsen & Schoeberl (1984) showed numerically that a small, locally unstable region of a zonal flow (where the gradient of ω_p is positive) evolves into a much larger region that is approximately marginally stable (where the gradient of ω_p is approximately zero). As a second example, Sommeria, Myers & Swinney (1988) showed experimentally that an external forcing that mixes the fluid also mixes and homogenizes the potential vorticity (whose governing equation is $D\omega_p/Dt \approx 0$ – see §2) so that zonal flows with approximately uniform ω_p are produced spontaneously. Of course, not all unstable or forced flows produce zonal velocities with uniform ω_p, but this class of flows is sufficiently common and produces vortex dynamics sufficiently rich and easy to interpret that it warrants study.

In §2 we present the equations of motion and describe their numerical solution. In §3 we demonstrate how the shear of a zonal flow breaks the degeneracy between clockwise and counterclockwise vortices; the vortex with the same sense of rotation as the zonal flow remains intact while the vortex with the opposite sign is stretched into a thin layer and breaks into small fragments or dissipates. In §4 we examine the breakup of a vortex layer in a zonal flow. We choose it as an example because it clearly demonstrates the transfer of energy between the self-energy of the vorticity and the interaction energy of the zonal flow with the vorticity. The behaviour of the layer depends on the direction in which the energy is transferred which depends in turn upon the sign of the vorticity of the layer with respect to the sign of the shear of the zonal flow. Vortex mergers are examined in §§4 and 5. We show how the potential vorticity rearranges itself inside a large vortex after smaller vortices bind together. We also show that vortices merge if and only if their initial separation in the cross-zonal direction is less than a critical value. Small-scale filaments of vorticity within the zonal flow are found to absorb energy from the large vortices, and we use this observation to predict the critical value for the initial separation between merging vortices. Our conclusions are presented in §6 where we also discuss future numerical work and the relationships among this work, laboratory experiments (Sommeria *et al.* 1988), and numerical work on long-lived planetary vortices (Marcus 1988).

2. Equations

2.1. *Equations of motion*

In this paper we consider two-dimensional, inviscid, constant-density, quasi-geostrophic flows. The fluid is contained in a rapidly rotating annulus bounded above by a flat impermeable surface at $z = 0$ and below by a smooth, axisymmetric, but not flat bottom at $z = -[H + h(r)]$, where H is the mean depth and $|h/H| \ll 1$. The velocity

$\boldsymbol{u}$ of this flow is two dimensional (perpendicular to $\hat{\boldsymbol{e}}_z$), divergence-free, and governed by a generalization of the Euler equation

$$\left(\frac{\partial}{\partial t} + (\boldsymbol{u} \cdot \boldsymbol{\nabla})\right) \boldsymbol{u} \equiv \frac{\mathrm{D}\boldsymbol{u}}{\mathrm{D}t} = -\frac{\boldsymbol{\nabla}\varPi}{\rho} + \boldsymbol{e}_z \times \frac{2\varOmega}{H} h(r)\,\boldsymbol{u} \qquad (2.1)$$

where $\varOmega\hat{\boldsymbol{e}}_z$ is the angular velocity of the rotating annulus, $\varPi$ is the pressure head of the flow, ρ is the density, and $\boldsymbol{u}$ is the velocity as observed in the rotating frame of the annulus. Equation (2.1) is equivalent to the shallow-water equation for a constant-density fluid and is valid for small Rossby number, $Ro \equiv U/2\varOmega L \ll 1$, where L and U are the characteristic magnitudes of the horizontal length and of $\boldsymbol{u}$. We have chosen an annular rather than the more standard planar geometry because it has a naturally periodic coordinate, hence no upstream or downstream boundary conditions. Moreover, the geometry will allow us to make a direct comparison with the laboratory experiments of Sommeria *et al.* (1988). The boundary conditions of the flow are that $u_r \equiv 0$ at $r = R_{\text{in}}$ and $r = R_{\text{out}}$. Note that (2.1) reduces to the Euler equation for $h \equiv 0$, and to the usual β-plane equations for $h \equiv \beta y$ or $h \equiv \beta r$.

Many of the simulations in this paper produce flows with more-or-less permanent, non-axisymmetric features, so a natural question to ask is how fast those features travel around the annulus. Because of the rotational invariance of equation (2.1) (i.e. if $\boldsymbol{u}(r, \phi, t)$ is a solution to (2.1), then so is $\boldsymbol{u}(r, \phi - Ct, t) + Cr\hat{\boldsymbol{e}}_\phi$, where C is arbitrary), this question does not have a unique answer. Therefore, when we refer to the rotational speed of a feature, it will be with respect to the surrounding zonal velocity. Another symmetry of (2.1) is that it is invariant under the transformation $\varOmega h(r) \to -\varOmega h(r)$, $\phi \to -\phi$, and $u_\phi \to -u_\phi$.

2.2. *Decomposition of the velocity*

The potential vorticity ω_{p} of $\boldsymbol{u}$ is defined as

$$\omega_{\mathrm{p}}(r, \phi, t) \equiv \boldsymbol{\nabla} \times \boldsymbol{u}(r, \phi, t) - 2\varOmega h(r)/H. \qquad (2.2)$$

The flows of interest to us in this paper have large regions of ω_{p} superposed on background axisymmetric zonal flows of nearly uniform potential vorticity. This suggests a decomposition of the flow into two components. We define the background zonal flow $\hat{\boldsymbol{v}}$ to be the exactly axisymmetric, azimuthal flow with uniform potential vorticity:

$$\hat{v}_\phi(r) \equiv \frac{2\varOmega}{rH} \int_{R_{\text{in}}}^{r} h(r')\,r'\,\mathrm{d}r' + C_1\,r + \frac{C_2}{r}, \qquad (2.3)$$

$$\hat{v}_r \equiv 0, \qquad (2.4)$$

where C_1 and C_2 are constants. The other component $\boldsymbol{v}$ is simply defined as $\boldsymbol{v} \equiv \boldsymbol{u} - \hat{\boldsymbol{v}}$. We denote the curl of $\boldsymbol{v}$ and $\hat{\boldsymbol{v}}$ as ω and $\hat{\omega}$ respectively, and we define the shear as σ and $\hat{\sigma}$:

$$\sigma(r, \phi, t) \equiv r\frac{\partial v_\phi/r}{\partial r} + \frac{1}{r}\frac{\partial v_r}{\partial \phi} \qquad (2.5)$$

and

$$\hat{\sigma}(r) \equiv r\frac{\partial \hat{v}_\phi/r}{\partial r}, \qquad (2.6)$$

Note that $\hat{v}$ is itself an exact equilibrium solution of (2.1). Equation (2.1) implies

$$\frac{\mathrm{D}\omega_{\mathrm{p}}}{\mathrm{D}t} = 0 \tag{2.7}$$

and because $\omega = \omega_{\mathrm{p}} - 2C_1$, it is also advectively conserved:

$$\frac{\mathrm{D}\omega}{\mathrm{D}t} = 0. \tag{2.8}$$

For the decomposition of u into $\hat{v}$ and v to be unique, the constants C_1 and C_2 must be specified. The choices of C_2 and C_1 are arbitrary, and we define them as

$$C_2 \equiv \frac{4\pi\Omega}{AH} \int_{R_{\mathrm{in}}}^{R_{\mathrm{out}}} h(r)\, r^3 \,\mathrm{d}r - \frac{2L^{\mathrm{tot}}}{\rho AH} - \frac{1}{2A}(\Gamma_{\mathrm{out}}^{\mathrm{tot}} R_{\mathrm{out}}^2 - \Gamma_{\mathrm{in}}^{\mathrm{tot}} R_{\mathrm{in}}^2), \tag{2.9}$$

$$C_1 \equiv \frac{1}{R_{\mathrm{in}}^2}\left(\frac{\Gamma_{\mathrm{in}}^{\mathrm{tot}}}{2\pi} - C_2\right), \tag{2.10}$$

where A is the area of the annulus that bounds the fluid, L^{tot} is the total angular momentum of u, and $\Gamma_{\mathrm{out}}^{\mathrm{tot}}$ and $\Gamma_{\mathrm{in}}^{\mathrm{tot}}$ are the circulations of u at R_{out} and R_{in}:

$$\Gamma_{\mathrm{out}}^{\mathrm{tot}} = \int_0^{2\pi} u_\phi(R_{\mathrm{out}}, \phi, t)\, r\, \mathrm{d}\Phi, \tag{2.11}$$

$$\Gamma_{\mathrm{in}}^{\mathrm{tot}} = \int_0^{2\pi} u_\phi(R_{\mathrm{in}}, \phi, t)\, r\, \mathrm{d}\phi. \tag{2.12}$$

The right-hand sides of (2.9) and (2.10) are time-independent, therefore $\hat{v}$ is time-independent. The definition of C_1 makes Γ_{in}, the circulation of the v-component of the velocity at R_{in}, equal to zero for all time. The definition of C_2 makes the average value of σ (weighted by r^2) zero for all time (see §2.3). All definitions of the decomposition lead to the same physical results, but these choices are very useful: we shall argue that the dynamics of a vortex embedded in a zonal flow depends upon the ratio of ω to the shear of the local zonal flow. With C_2 defined by (2.9), the shear of the surrounding zonal flow is approximately $\hat{\sigma}$. The definition of C_1 leads to a simple relationship between the kinetic energies and ω (see §2.3).

2.3. Conserved quantities

Equation (2.1) conserves angular momentum, energy, two independent circulations, and all moments of the enstrophy.

The circulation $\Gamma^{\mathrm{tot}} \equiv \Gamma_{\mathrm{out}}^{\mathrm{tot}} - \Gamma_{\mathrm{in}}^{\mathrm{tot}}$ is conserved, and it can be written in terms of ω:

$$\Gamma^{\mathrm{tot}} = \int_D \omega(r, t)\, r\, \mathrm{d}r\, \mathrm{d}\phi + \Gamma_0, \tag{2.13}$$

where D is the domain of the annulus and Γ_0 is the time-independent constant

$$\Gamma_0 = 2AC_1. \tag{2.14}$$

(We have used the fact that the mean depth of the annulus H is defined such that $\int_{R_{\mathrm{in}}}^{R_{\mathrm{out}}} h(r)\, r\, \mathrm{d}r \equiv 0$.) Therefore $\omega(r, t)$ integrated over the domain of the fluid is conserved.

The angular momentum L^{tot} is

$$L^{\mathrm{tot}} = -\tfrac{1}{2}\rho H \int_D r^2 \omega(\mathbf{r}, t) \, r \, \mathrm{d}r \, \mathrm{d}\phi + L_0, \tag{2.15}$$

where L_0 is the time-independent constant

$$L_0 = \tfrac{1}{2}\rho H[\Gamma^{\mathrm{tot}}_{\mathrm{out}} R^2_{\mathrm{out}} - \Gamma^{\mathrm{tot}}_{\mathrm{in}} R^2_{\mathrm{in}}] - \tfrac{1}{2}\rho H A C_1 [R^2_{\mathrm{out}} + R^2_{\mathrm{in}}] - 2\pi\rho\Omega \int_{R_{\mathrm{in}}}^{R_{\mathrm{out}}} r^3 h(r) \, \mathrm{d}r. \tag{2.16}$$

Equation (2.15) shows that the ω-weighted value of r^2 is conserved in time. Conservation of angular momentum and circulation imply conservation of $r^2\sigma$, and with our choice of C_2

$$\int_D r^2 \sigma(\mathbf{r}, t) \, r \, \mathrm{d}r \, \mathrm{d}\phi \equiv 0. \tag{2.17}$$

The conserved kinetic energy is

$$E^{\mathrm{tot}} \equiv \tfrac{1}{2}\rho H \int_D u^2 r \, \mathrm{d}r \, \mathrm{d}\phi \equiv E^{\mathrm{self}}(t) + E^{\mathrm{int}}(t) + E_0, \tag{2.18}$$

where E^{self} is quadratic in $\mathbf{v}$:

$$E^{\mathrm{self}}(t) \equiv \tfrac{1}{2}\rho H \int_D v^2 r \, \mathrm{d}r \, \mathrm{d}\phi = -\tfrac{1}{2}\rho H \int_D \omega(\mathbf{r}, t) \, \psi(\mathbf{r}, t) \, r \, \mathrm{d}r \, \mathrm{d}\phi. \tag{2.19}$$

E^{int} is linear in $\mathbf{v}$:

$$E^{\mathrm{int}}(t) \equiv \rho H \int_D \mathbf{v} \cdot \hat{\mathbf{v}} \, r \, \mathrm{d}r \, \mathrm{d}\phi = -\rho H \int_D \omega(\mathbf{r}, t) \, \hat{\psi}(r) \, r \, \mathrm{d}r \, \mathrm{d}\phi, \tag{2.20}$$

and E_0 is the time-independent constant

$$E_0 = \tfrac{1}{2}\rho H \int_D \hat{v}^2 r \, \mathrm{d}r \, \mathrm{d}\phi. \tag{2.21}$$

Here $\psi(\mathbf{r}, t)$ and $\hat{\psi}(r)$ are the stream functions of $\mathbf{v}$ and $\hat{\mathbf{v}}$ respectively and their gauges are chosen so $\psi(R_{\mathrm{out}}) = \hat{\psi}(R_{\mathrm{out}}) \equiv 0$. Without this choice of gauge and our definition of C_1, the expressions for E^{self} and E^{int} would contain time-dependent surface terms.

The self-energy $E^{\mathrm{self}}(t)$ is the energy that the flow $\mathbf{v}$ would have if $\hat{\mathbf{v}} \equiv 0$. For example, in the absence of horizontal boundaries $E^{\mathrm{self}}(t)$ is (up to an additive constant)

$$E^{\mathrm{self}}(t) = -\frac{\rho H}{4\pi} \int_D \int_{D'} \ln|\mathbf{r} - \mathbf{r}'| \, \omega(\mathbf{r}, t) \, \omega(\mathbf{r}', t) \, r \, \mathrm{d}r \, \mathrm{d}\phi \, r' \, \mathrm{d}r' \, \mathrm{d}\phi'. \tag{2.22}$$

The self-energy of the flow is completely analogous to the self-energy of a distribution of electric charge (in two dimensions). The self-energy of two vortices increases logarithmically with the distance between them; pushing two vortices (or charges) of the same sign together increases E^{self} and requires external work. A single uniform vortex with fixed area is in its highest energy state when its shape is round; any elongation reduces its self-energy. Because a boundary can be conceptually replaced by an image vortex of equal and opposite sign on the opposite side of the boundary, it is clear that moving a vortex closer to a boundary (and hence closer to its opposite-

signed image) decreases E^{self}. The term $E^{\text{int}}(t)$ is the interaction energy between the v- and $\hat{v}$-components of the velocity. It is analogous to the interaction energy between a charge of strength ω in an electrostatic potential $\hat{\psi}(r)$. Although E^{self} is invariant under the transformation $\omega \rightarrow -\omega$, E^{int} is not. This is why vortex dynamics with no background flow is degenerate with respect to the sign of ω and why stable vortices have a preferred sign when $\hat{v}$ is present.

The nth moment of the enstrophy $\mathscr{E}_n$ based on ω is conserved:

$$\mathscr{E}_n \equiv \int_D \omega(\mathbf{r}, t)^n \, r \, \mathrm{d}r \, \mathrm{d}\phi. \tag{2.23}$$

If $h(r) \neq 0$, the enstrophies made from the total vorticity, $\nabla \times \mathbf{u}$, are not conserved.

2.4. Numerical methods

The nonlinear solutions to (2.1) that are presented throughout this paper are computed with an initial-value code that uses a spectral collocation method with 256×256, 128×128, or 64×64 Fourier–Chebyshev modes. Our numerical computations are carried out in a constantly changing rotating frame so that the effective Courant number is minimized. Details of the numerics and the types of tests that the numerical codes were subjected to were reported for a similar calculation earlier (Marcus 1984a). In this paper we compute two types of solutions. In the first, we solve (2.1) with no numerical dissipation. The energy, angular momentum, and each of the two independent circulations are conserved from the beginning to the end of a run to one part in 10^6. The second moment of the enstrophy, which cascades more quickly than the energy to the small scales, is conserved only to one part in 10^4. The spectral calculations are terminated when enough enstrophy builds up at the smallest numerically resolvable scale that the enstrophy spectrum begins to turn upward. The time that it takes for the enstrophy spectrum to turn upward depends on the initial conditions. Frequently it is many dynamical times, and the physics that we need to observe takes place well before the computation needs to be terminated. Occasionally, we need to run for longer times. The proper and only numerically sound way of solving this problem is to repeat the calculation with more resolution so that it takes longer for the enstrophy to cascade to the smallest resolvable scale. However, we have found empirically that removing the aliasing errors retards the pile-up of enstrophy at small scales and allows us to run the calculations for a slightly longer time while maintaining accuracy. (As a test we compared the de-aliased results with calculations with twice the numerical resolution and found good agreement.) Therefore the calculations reported in this paper have been de-aliased using the '$\frac{3}{2}$-rule' (see Orszag 1974). This benefit from de-aliasing is in contrast to our experience with spectral collocation methods in a similar geometry when the Navier–Stokes equation is solved. There we found that the small-scale viscous dissipation dominated the aliasing and solutions computed with and without aliasing were indistinguishable from each other (Marcus 1984b).

In any case, de-aliasing can postpone the pile-up of enstrophy at the small scales but it cannot get rid of it. A second method for computing solutions at late time is to add dissipation to the code. We have tried four types of dissipation: hyperviscosity or $\nabla^4 \mathbf{u}$, molecular viscosity, Ekman spin-down, and direct removal of energy from the highest wavenumber Fourier–Chebyshev modes. Results obtained using a hyperviscosity and direct removal from the highest modes were indistinguishable at the large scales. Because hyperviscosity was more expensive and cumbersome to

implement (the equation requires two more radial boundary conditions), results reported here were computed by the direct removal method. Molecular viscosity and Ekman spin-down made the energy decay quickly in these run-down experiments. These sources of dissipation correspond to those in the laboratory experiments of Sommeria *et al.*, and we report our results with these sources of dissipation elsewhere.

In our calculations with dissipation the circulation and momenta are still conserved to about 1 part in 10^6, and the energy to 1 part in 10^3, but the enstrophy can decrease by as much as 30%. We have compared solutions made with no dissipation to solutions that were computed with dissipation and with half the number of Fourier–Chebyshev modes. For times that are long enough that the low-resolution calculation is dissipative but short enough that the non-dissipative, high-resolution calculation does not have an appreciable upward turn in its enstrophy spectrum, the two solutions are nearly identical for all but the smallest scale modes. We therefore believe that the large-scale physics is accurately represented in our weakly dissipative calculations.

In this paper we illustrate the flows with false-colour plots where each pixel has a colour that represents the local value of ω, with red for the most positive value of ω, blue for the most negative, and the colours as ordered in the spectrum for the intermediate values. Each pixel represents an average of ω over the area of the pixel, so if the pixel size were less than or equal to the numerical resolution, each pixel would act like a fluid element and be advected by the local velocity, conserving its colour or value of ω. However, our pixels range in size from 4 to 64 times larger than the numerical resolution. Thus pixel colour is not conserved. The averaging blurs small-scale structures. For example, it makes a region that contains fine filaments of red and blue ω appear as green.

Throughout the remainder of the paper we shall use dimensionless units in which the density is in units of ρ, horizontal length in units of $(R_{out} - R_{in})$, vertical depth or $h(r)$ in units of H, and time in units of $\frac{1}{2}\Omega$.

3. Sign-dependent behaviour of vortices

3.1. *Initial dipolar stream function*

To demonstrate how the behaviour of vortices in a shearing zonal flow depends upon the sign of $\hat{\sigma}/\omega$, we choose an initial flow consisting of one large vortex of each sign superposed on the zonal flow

$$\hat{v}_\phi = \tfrac{1}{6}r(2r - R_{in} - R_{out}). \tag{3.1}$$

The bottom topography is $h(r) = (r - \tfrac{5}{6})$, and $R_{in}/R_{out} = 0.25$. Note that $\hat{\sigma} = \tfrac{1}{3}r > 0$ and that $\hat{v}_\phi = 0$ midway between the inner and outer annular boundaries. The zonal flow in (3.1) was chosen because it has a non-zero $\hat{\sigma}$ and a non-trivial (i.e. non-constant) $\hat{\omega}$.

The initial vortices in figure 1 (*a*) (plate 1) have the stream function

$$\psi(r, \phi) = g(r, \phi + \tfrac{1}{2}\pi) - g(r, \phi - \tfrac{1}{2}\pi), \tag{3.2}$$

where $$g(r, \phi) = 0.01 \sin^2\left[\pi(r - R_{in})\right]\left[\sin\left(\tfrac{1}{2}\phi\right)\right]^{32}. \tag{3.3}$$

The large exponent in the ϕ-dependence of the stream function was chosen because it produces two large vortices of nearly uniform ω with sharp, but numerically resolvable, boundaries. The maximum and minimum values of ω are ± 0.34, so $|\hat{\sigma}/\omega| = O(1)$ at the centres of the two large vortices. The four smaller banana-shaped

vortices that initially surround the two large vortices were included as part of the initial conditions because they allow us to illustrate the effects of the boundaries. Our calculations were done with a small amount of dissipation in the eight smallest Fourier–Chebyshev modes.

3.2. Focusing and expulsion of ω

Figure 1 $(b-h)$ (plates 1, 2) shows the subsequent flow with the times listed in the caption given in units of the approximate turn-around time of the large vortices, $0.34/4\pi$. Each large vortex is initially pulled apart by $\hat{v}_\phi$ which is clockwise near the inner boundary and counterclockwise near the outer (figure 1b). Even at early times, there is a large asymmetry between the red and blue vortices. As the red vortex with $\hat{\sigma}/\omega > 0$ is stretched azimuthally, it remains midway between the inner and outer boundaries, whereas the extremities of the blue vortex are pulled to the two radial boundaries (figure 1c). This effect is easily understood by using the fact that the total velocity at any location can be found from the plot of ω in figure 1 by adding the velocity due to ω – using the usual Biot–Savart law – to $\hat{v}_\phi$. In figure 1 (b) a fluid element with red ω located at the outer edge of the large red vortex is first pulled counterclockwise by $\hat{v}_\phi$ towards the right-hand side of the vortex. The counterclockwise velocity produced by the vorticity of the red vortex itself then pushes this fluid element inward towards the inner radius. Thus an element located initially at the outer edge of the vortex is pushed towards the inner boundary. Similarly, an element located initially at the inner edge of the vortex is pushed towards the outer boundary. A fluid element with blue ω located at the outer edge of the large blue vortex will be pulled counterclockwise by $\hat{v}_\phi$ towards the left-hand side of the blue vortex. The clockwise velocity of the blue vortex will then push the element outward towards the outer radius. A fluid element of blue ω located initially at the outer edge of the blue vortex is drawn further outwards by the combined interaction of $\hat{v}_\phi$ and the velocity of the blue vortex, and an element located initially at the inner edge of the blue vortex is pushed further inward towards the radial boundary. Thus, a vortex with $\hat{\sigma}/\omega < 0$ is stretched into a spiral and its vorticity is pulled towards the radial boundaries of the shearing zonal flow; whereas a vortex with $\hat{\sigma}/\omega > 0$ is focused towards the centre of the zonal flow. This focusing and expulsion is further examined in §3.9.

3.3. Breakup of vortex layers

Figure 1 (c) shows that the large blue vortex is surrounded on each side by thin yellow spirals that are the remnants of the two initial, banana-shaped, yellow vortices. The yellow vortex layers with $\hat{\sigma}/\omega > 0$ break up into modes whose wavelengths are approximately 16 times their thickness (figure 1$c-f$). (In §4 we show that this wavelength is the most rapidly growing unstable Kelvin–Helmholtz eigenmode of the yellow vortex layer in figure 1c.) As the two yellow layers break up, they disrupt the blue spiral and cause it to fragment. After 6 turn-around times the blue spiral is broken into small thin filaments (figure 1g).

3.4. Robustness of vortices with $\hat{\sigma}/\omega > 0$

The large red vortex is sheared azimuthally until ~ 0.7 turn-around times and then contracts. During this time it sheds a small amount of ω ($\approx 5\%$ of its circulation). Some of the shed fragments become uniformly dispersed in the zonal flow, some go into the radial boundary layers, but more than half eventually reattach to the large red vortex. Figure 1 (g) shows that in just six turn-around times the flow has formed

one large, approximately elliptically shaped, red vortex and a much smaller red vortex near the inner boundary that is distinctly separated in radial location from the large one. The large vortex has an approximately permanent form and travels azimuthally around the annulus at an approximately constant velocity (see below), but it is not a steady state. It is buffeted about with respect to its mean velocity by the blue filaments of ω, and its shape and size are not permanent because it constantly sheds and regains filaments of ω. After six turn-around times all of the blue ω that was initially located in large vortices is fragmented into small pieces, and it ends up in one of three places: in the inner or outer radial boundary layers or as thin filaments of ω that are spread approximately uniformly throughout the flow. (The amount at each location is discussed in §5.) The uniform spreading of the blue filaments in the zonal flow is an example of the homogenization of potential vorticity discussed in §1. The motion of the blue filaments is chaotic, and a power spectrum of the velocity shows broad peaks.

Figure 1 (h) shows that the flow after 20 turn-around times is still quite similar to the flow in figure 1 (g) with the exception that the flow surrounding the two red vortices has lost most of its small-scale structure; the flow in figure 1 (h) has the same circulation and angular momentum (to within 10^{-4} %) as in figure 1 (g) but has less than ~ 30 % of the enstrophy because the numerical dissipation smooths the nearly uniform distribution of thin blue filaments into a zonal flow with nearly uniform ω. The *macroscopic* velocities in figure 1 (g, h) are the same to within 8 %. Here, and throughout the remainder of this paper we define a *macroscopic* quantity by construction: filter out the highest spatial modes and average over one turn-around time.

3.5. *Advected velocities of vortices*

Travelling waves or vortices of permanent forms superposed on zonal flows do not, in general, advect at the speed of the local flow velocity, cf. the solitary Rossby wave solutions of Maxworthy & Redekopp (1976). However, vortices with boundaries defined by closed isopotential vorticity contours do. To see this, define the location of an arbitrary distribution of vorticity X_ω as

$$X_\omega \equiv \frac{\int \omega r r \, \mathrm{d}r \, \mathrm{d}\phi}{\int \omega r \, \mathrm{d}r \, \mathrm{d}\phi}, \tag{3.4}$$

and its velocity V_ω as $\mathrm{D}X_\omega/\mathrm{D}t$, or

$$V_\omega \equiv \frac{\mathrm{D}X_\omega}{\mathrm{D}t} = \frac{\int \omega u r \, \mathrm{d}r \, \mathrm{d}\phi}{\int \omega r \, \mathrm{d}r \, \mathrm{d}\phi} = \hat{V}_\omega + \frac{\oint v(v \cdot \mathrm{d}s) - \oint \frac{1}{2} v^2 \, \mathrm{d}s}{\int \omega r \, \mathrm{d}r \, \mathrm{d}\phi}, \tag{3.5}$$

where

$$\hat{V}_\omega \equiv \frac{\oint \omega \hat{v} r \, \mathrm{d}r \, \mathrm{d}\phi}{\int \omega r \, \mathrm{d}r \, \mathrm{d}\phi}. \tag{3.6}$$

The integrals in (3.4)–(3.6) must be taken over the entire domain or over a region bounded by a closed material curve – for example, a closed contour with a constant
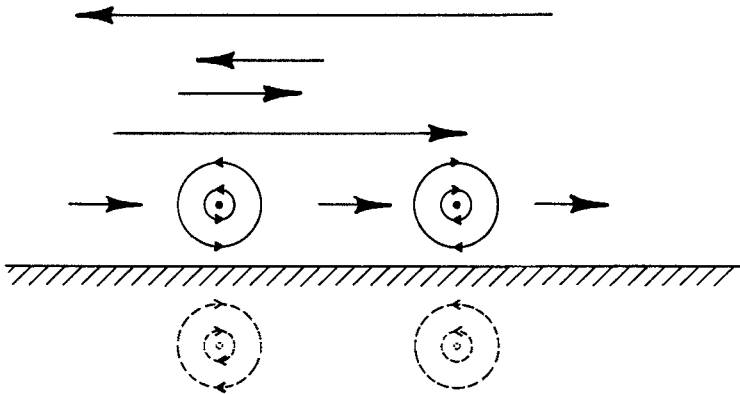
FIGURE 2. Sketch showing how a counterclockwise vortex with $\hat{\sigma}/\omega > 0$ (at the left of the figure) overtakes a clockwise vortex with $\hat{\sigma}/\omega < 0$ (at the right). $\hat{v}$ (represented by the long straight arrows) advects both vortices to the right at the same velocity. The image vortices (dashed streamlines) below the boundary increase the velocity of the vortex with $\hat{\sigma}/\omega > 0$ and retard the motion of the vortex with $\hat{\sigma}/\omega < 0$.

value of ω. If there are no horizontal boundaries, it is often useful to use the entire domain because the two contour integrals in (3.5) vanish, and then $V_\omega = \hat{V}_\omega$. For a flow with one or more isolated compact patches of vorticity, the integrals could be taken over one of the patches. Then, V_ω is the sum of $\hat{V}_\omega$ (which is $\hat{v}$ averaged over the area of the vortex) and the two contour integrals (which are the velocity due to the advection by the other patches of vorticity and the velocity due to the boundaries – which could be replaced with image vortices). Thus in figure 1 (h), each of the two vortices moves approximately at the speed of its local $\hat{v}$ (which are not the same). In §5 we show that if more than one vortex is present at late times, then each vortex must be located at a different radial location. Therefore in general, if $\partial \hat{v}_\phi / \partial r \neq 0$, each vortex travels around the annulus at a unique speed.

Figure 1 shows that the small red and blue vortices near the inner boundary are both advected clockwise by $\hat{v}_\phi$ but that the red vortex with $\hat{\sigma}/\omega > 0$ travels faster and eventually overtakes the blue vortex with $\hat{\sigma}/\omega < 0$. This overtaking can be understood by examining the sketch of the inner boundary (using a plane-parallel approximation) in figure 2. Both small vortices (indicated by solid streamlines) are advected to the right by the same $\hat{V}_\omega$. (The $\hat{v}$ is indicated by the arrows pointing to the right near the boundary at the middle of the figure and to the left at the top of the figure.) The effect of the boundaries is to produce image vortices (shown as broken streamlines beneath the boundary). The image retards the motion of the blue vortex with $\hat{\sigma}/\omega < 0$ but aids the motion of the red vortex with $\hat{\sigma}/\omega > 0$. Therefore the vortex with $\hat{\sigma}/\omega > 0$ overtakes the vortex with $\hat{\sigma}/\omega < 0$.

3.6. Spectra

During the first few time-around times of the flow's evolution some kinetic energy is transferred from large scales to smaller scales, but most remains in the large scales. The energy spectra $E(m)$ as a function of azimuthal wavenumber m after 0, 6.03, and 20.7 turn-around times are shown in figure 3. This is the spectrum for a calculation with 128 de-aliased Fourier modes in the azimuthal direction, but there was
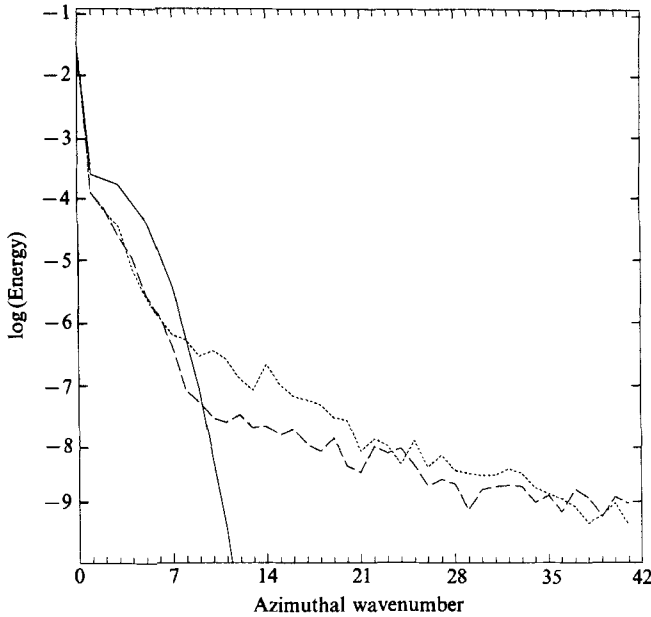
FIGURE 3. Energy spectrum $\log_{10} E(m)$ of the flow in figure 1. Solid curve after 0 turn-around times (figure 1a), dotted curve after 6.04 (figure 1g), and long-dashed curve after 20.7 (figure 1h).

essentially no change in this part of the spectrum when the calculation was repeated with 256 modes. The spectrum $E(m)$ is defined

$$E(m) \equiv \tfrac{1}{2}\pi(1 + \delta_{m,0}) \int_{R_{\text{in}}}^{R_{\text{out}}} |u(r,t)_m|^2 r \, \mathrm{d}r, \qquad (3.7)$$

so

$$E = \sum_{m=0}^{M} E(m) \qquad (3.8)$$

where $u(r, t)_m$ is the mth azimuthal Fourier component of $u(r, \phi, t)$. In figure 3 we have connected the *non-zero* values of $E(m)$ with a solid line. (NB Except for $m = 0$, the initial energy spectrum is zero for all even values of m and for all $m > 16$.) Although the flow represented in figure 3 does not show a reverse energy cascade (as many of our flows do – see §5) most of the kinetic energy remains trapped in the large-scale modes. For $m \geqslant 10$, the late-time spectrum of the flow in figure 1 has $E(m) \propto m^{-4}$ consistent with the high-resolution, two-dimensional simulations of vortex-dominated flows computed by Benzi, Patarnello & Santngelo (1987).

3.7. *Family of solutions*

We have repeated our numerical calculations with the same bottom topography and zonal flow as in (3.1) but with the initial dipolar stream function given by (3.2) and (3.3) multiplied by a constant. By varying the value of the constant we computed a family of solutions in which the magnitude of the vorticity ω varies with respect to the magnitude of the $\hat{\sigma}$. Because neither ω nor $\hat{\sigma}$ is uniform throughout the flow, we arbitrarily define a vortex's characteristic vorticity $\langle \omega \rangle$ as its maximum or minimum value and the characteristic zonal shear $\langle \hat{\sigma} \rangle$ as the value of $\hat{\sigma}$ at the location where

the initial vortex has its maximum amplitude. We have explored the range $10 > |\langle\hat{\sigma}\rangle/\langle\omega\rangle|$. There are four regimes – two of which are examined in this paper: the regime $|\langle\hat{\sigma}\rangle/\langle\omega\rangle| > 4$ is not of interest to us in this paper because initial vortices of both sign are stretched into thin spirals that break apart. The regime $|\langle\hat{\sigma}\rangle/\langle\omega\rangle| \leqslant 0.1$ is also not of interest to us because the vortices behave as if there were no zonal flow present, and this behaviour has been reported elsewhere. For $4 > |\langle\hat{\sigma}\rangle/\langle\omega\rangle| > 0.2$, we find that the vortices behave similarly to those in figure 1 which have $\langle\hat{\sigma}\rangle/\langle\omega\rangle = \pm 0.8$. In particular, for the eight flows that we examined in this range we found that within one turn-around time the vortex with $\langle\hat{\sigma}\rangle/\langle\omega\rangle < 0$ always stretches into a spiral whose extremities are drawn to the radial boundaries. After one to three turn-around times the spiral fragments into filaments of ω that are either deposited at the radial boundaries or are mixed uniformly throughout the zonal flow. The vortex with $\langle\hat{\sigma}\rangle/\langle\omega\rangle > 0$ remains nearly intact shedding only 3–10% of its vorticity. This vortex oscillates, alternately stretching and contracting in the azimuthal direction. The oscillations damp in 5–10 turn-around times, and the flow reaches a statistically steady state. Most of the ω shed during the oscillations is reattached to the vortex. A second example of a solution in this regime is shown in figure 4 (plate 3) after 62.1 turn-around times. Here $\langle\hat{\sigma}\rangle/\langle\omega\rangle = 0.28$. This late-time flow is quite similar to the one in figure 1 (h). The main differences between the two are that in figure 4 the small red vortex initially at the inner boundary has merged with the large red vortex, and the large vortex in figure 4 is much rounder than the one in figure 1 (h). (The merging is discussed in §5.) We parameterize the shape with ϵ which we define to be the ratio of the length of the macroscopic vortex in its azimuthal direction to that in the radial, where we arbitrarily define the boundary of the vortex to be the isovorticity contour with $|\omega| = 0.1|\langle\omega\rangle|$. Not surprisingly, we find that ϵ increases with $\langle\hat{\sigma}\rangle/\langle\omega\rangle$ owing to the stretching of the vortex by the zonal shear.

The regime $0.1 < |\langle\hat{\sigma}\rangle/\langle\omega\rangle| < 0.2$ is different from the previous regime because here vortices of both sign exist and are stable. Vortices of both sign are approximately round ($\epsilon = 1$), but the ϵ of the vortex with $\langle\hat{\sigma}\rangle/\langle\omega\rangle > 0$ is always greater than that of the vortex with $\langle\hat{\sigma}\rangle/\langle\omega\rangle < 0$. Except for vortices located initially very close to a boundary, a vortex with $\langle\hat{\sigma}\rangle/\langle\omega\rangle < 0$ has $\epsilon < 1$. The vortices with $\langle\hat{\sigma}\rangle/\langle\omega\rangle < 0$ are less robust than those with $\langle\hat{\sigma}\rangle/\langle\omega\rangle > 0$, as our simulations show that they can be broken into fragments by perturbations. To illustrate exactly how we perturbed the vortices consider figure 5 which is a schematic of the streamlines of an unbounded steady-state vortex with $\langle\hat{\sigma}\rangle/\langle\omega\rangle < 0$. Here, streamlines are either closed and bounded, or they are open and extend to infinity. In contrast, an unbounded vortex with $\langle\hat{\sigma}\rangle/\langle\omega\rangle > 0$ has only closed streamlines. The streamlines near the vortex are closed, and the last closed streamline or separatrix (shown by a broken curve in figure 5) connects two stagnation points. Velocities along streamlines inside the separatrix have circulations with the same sign as the vortex; outside, they have the opposite sign. Imagine perturbing the flow by perturbing the boundary of the vortex so that the circulation, angular momentum and enstrophy remain fixed. If the perturbation is small, then the location of the separatrix remains nearly constant. Clearly, any piece of the vortex that is perturbed outside the separatrix can never return across the separatrix and is carried off to infinity. The flow cannot return to its original equilibrium or even a close approximation of it. However, if the boundary of the perturbed vortex remains inside the separatrix, then all the ω is confined within the separatrix, and the vortex can relax back to a state close to its original equilibrium.
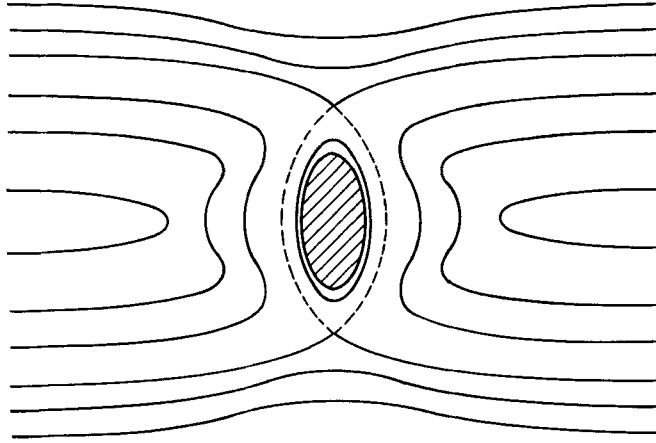
FIGURE 5. Sketch of streamlines of a steady-state flow consisting of a vortex with $\hat{\sigma}/\omega < 0$ (shaded region) and a non-zero $\hat{v}$. The two stagnation points exterior to the shaded region are connected by the last closed streamline or separatrix, shown as a broken curve. Inside the separatrix, the velocities along the closed streamlines have the same sign as the circulation of the vortex. Outside, the circulations of the velocities along the open streamlines have the opposite sign.

(By conservation of energy it cannot return to its original equilibrium.) Thus the distance between the boundary of the vortex and the separatrix sets the scale for the size of the finite-amplitude perturbations to which the vortex is unstable. To examine this perturbation numerically we added a perturbation to the vortex that conserved the flow's angular momentum, circulation and all enstrophy moments. In addition, the perturbation had a well-defined lengthscale. (The perturbed vortex is created numerically by integrating forward in time the equation

$$\frac{\partial \omega}{\partial t} = -\bar{v}_\phi(r)\frac{1}{r}\frac{\partial}{\partial \phi}\omega,$$

with the initial flow equal to the unperturbed macroscopic vortex and with $\bar{v}_\phi(r)$ equal to a Gaussian peaked midway between the inner and outer boundaries. This integration creates a perturbed vortex with a 'finger' growing out of its side in the azimuthal direction. The lengthscale of the perturbation is the length of the finger and is proportional to the time at which we integrate the equation. The integration clearly conserves the angular momentum, the two circulations, and all of the enstrophy moments of the original flow.) Our numerical simulations confirm the fact that the lengthscale of the perturbation that first causes a vortex to break apart is approximately equal to the distance between the separatrix and the edge of the unperturbed, equilibrium vortex.

We summarize our results by noting that the function $\epsilon(\langle\hat{\sigma}\rangle/\langle\omega\rangle)$ looks qualitatively like the curve shown in figure 6 which is the exact relation for an elliptical vortex of uniform strength $\langle\omega\rangle$ in an unbounded, plane-parallel zonal flow with uniform shear $\langle\hat{\sigma}\rangle$ (Moore & Saffman 1971). Not surprisingly, the $\epsilon(\langle\hat{\sigma}\rangle/\langle\omega\rangle)$ curve for our numerical family of solutions changes if we change our (arbitrary) definitions of the vortices' $\langle\omega\rangle$, or $\langle\hat{\sigma}\rangle$, or if we redefine the boundary at which ϵ is measured. However, all of the definitions that we tried show that ϵ increases
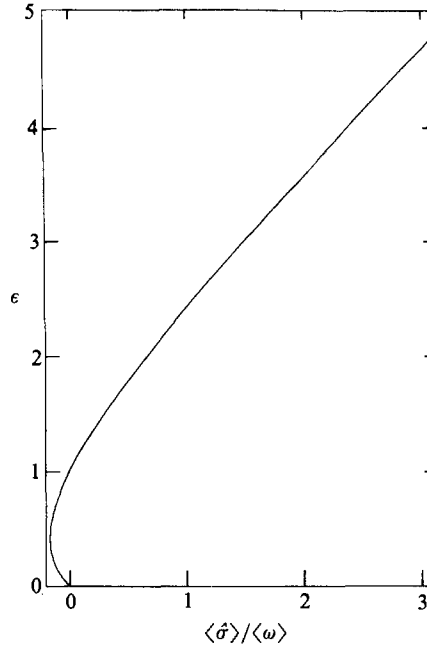
Figure 6. Relation between ϵ and $\langle\hat{\sigma}\rangle/\langle\omega\rangle$ for a Moore–Saffman ellipse with uniform vorticity $\langle\omega\rangle$ and $\hat{v} = -\langle\hat{\sigma}\rangle y\hat{e}_x$. $\epsilon = (1+\langle\hat{\sigma}\rangle/\langle\omega\rangle)f(\langle\hat{\sigma}\rangle/\langle\omega\rangle)$, where $f(\chi) \equiv \{1+\chi\pm[(1+\chi)^2+4\chi]^{\frac{1}{2}}\}/2(1+\chi)$. There are equilibria with $\langle\hat{\sigma}\rangle/\langle\omega\rangle < 0$ but there is a turning point so that there are none with $\langle\hat{\sigma}\rangle/\langle\omega\rangle < -3+2\sqrt{2}$.

monotonically with $\langle\hat{\sigma}\rangle/\langle\omega\rangle$, and all show a turning point near $\langle\hat{\sigma}\rangle/\langle\omega\rangle = -0.2$. Near the turning point we always find that the curve has the usual parabolic behaviour. With our initial-value code, of course, we have not been able to compute the unstable lower branch in figure 6.

Obviously, the $\epsilon(\langle\hat{\sigma}\rangle/\langle\omega\rangle)$ curve in figure 6 could not extend indefinitely to the left because the distance between the separatrix and the edge of the vortex decreases with decresing $\langle\hat{\sigma}\rangle/\langle\omega\rangle$. For sufficiently negative values of $\langle\hat{\sigma}\rangle/\langle\omega\rangle$, a vortex would overflow its own separatrix and could not be a steady equilibrium. The curve for the Moore–Saffman vortices has a turning before the distance between the vortex and the separatrix decreases to zero. Our family of vortices also has this property. However, we must note that we have found zonal flows in which a family of vortices extends to sufficiently negative values of $\langle\hat{\sigma}\rangle/\langle\omega\rangle$ that the vortex touches its own separatrix. At this point physically realizable solutions end abruptly, and the streamline that marks the boundary of the vortex develops a discontinuity in its slope. (With contour dynamics a 'corner' forms.) Examples of this latter case will be presented elsewhere.

3.8. *Relaxation to equilibrium in a nearly dissipationless flow*

The vortices examined in the last section relax from their initial non-equilibrium state to a statistically steady flow in a few turn-around times. Although the vortices initially oscillate, they damp quickly. It seems paradoxical that fast damping and relaxation to an equilibrium can occur in a nearly dissipationless flow. The explanation of the paradox is that although the total energy of the flow is conserved within 0.1 %, the energy of the large red vortex in figure 1 (defined to be the integral

of $\frac{1}{2}(\boldsymbol{u} \cdot \boldsymbol{u})$ over the domain enclosed by the $|\omega| = 0.1|\langle \omega \rangle|$ isovorticity contour) is not conserved. It decreases by $\sim 7\%$ after 6 turn-around times. This energy loss causes the damping. Although some of the energy loss is due to the shedding of vorticity with $\omega > 0$, we find numerically that over 80% goes into the energy of the blue, $\omega < 0$, vortex filaments.

To see how important the blue vortex filaments are in allowing the red vortex to relax to its equilibrium, we conducted two new numerical experiments. In the first, we repeated the numerical simulation of figure 1(a) with the following exception: all of the initial fluid elements in figure 1(a) not within the boundary of the large red vortex have their ω set equal to zero. That is, the initial distribution of vorticity in this new experiment looks like the large red vortex figure 1(a) but without the two small red vortices and with no blue or yellow vortices. In this simulation, the large red vortex is stretched azimuthally by $\hat{v}$ and oscillates. After 10 turn-around times it has lost less than 1% of its energy (owing to vortex shedding) and the oscillations have not noticeably damped. Our second new experiment is a repeat of the previous one with the exception that a uniform distribution of blue filaments of ω is added to the initial flow. (The filaments are created with a Fourier–Chebyshev series with random-phase coefficients Gaussianly distributed around a large radial and azimuthal wavenumber. The velocity is then transformed into physical space and filtered with a Gaussian peaked at $\omega = -0.3$.) In this experiment the oscillations of the large red vortex are damped. After 10 turn-around times the vortex loses over 6% of its initial energy to the blue filaments, and the macroscopic vortex is steady.

Thus for this family of vortices, we argue that the large coherent vortex relaxes to equilibrium by transferring energy to the small-scale, temporally chaotic, fluid filaments of ω rather than by vortex shedding. We have shown that the dynamics of vortices qualitatively differs if the vortices cannot lose their energy and thereby relax to equilibrium.

Because the filaments of vorticity with $\hat{\sigma}/\omega < 0$ promoted the fast relaxation of the large vortex with $\hat{\sigma}/\omega > 0$ to its equilibrium, we were curious whether the final equilibrium was a function only of the values of the conserved quantities listed in §2 and whether the flow lost the memory of all of the other properties of its initial condition. (The answer to this question is of importance to anyone who attempts to use statistical mechanics to predict final equilibria.) To answer this question we repeated the experiment shown in figures 4 and 1(a) five times, each time varying the initial radial location of the large blue and red vortices from $r = 0.75[\frac{1}{2}(R_{in} + R_{out})]$ to $r = 1.25[\frac{1}{2}(R_{in} + R_{out})]$. We also varied the initial azimuthal separation between the blue and red vortices so that the energies, momenta, circulations, and enstrophies of the five flows were the same. (By symmetry, the circulation, $\int \omega r^3 \, dr \, d\phi$, and E^{int} were zero for all five flows. The initial azimuthal separations were chosen to make the energies the same to one part in 10^5. Because the initial vortices were approximately isolated we expected that changes in their initial locations would have little effect on the flows' enstrophies, and we found this to be true; the first three moments of the enstrophies of the five flows differed by less than one part in 10^3.) Each of the five flows evolved to form one large red vortex, but the vortex's final radial location was not the same for all five flows and in each case was approximately equal to its initial value. Thus for these flows, the final equilibria were not just functions of the conserved quantities; the flows retained the memories of the initial locations of the large red vortices. (In other flows where the evolution is less laminar and where there is more mixing, the final flow does depend only on the values of the conserved quantities and loses memory of the original vortex locations – see §5.4.)

Finally, we note that we have repeated all of the numerical experiments in this section with a flat bottom topography and with

$$\hat{v}_\phi = \frac{R_{out} + R_{in}}{12}\left[r - \frac{(R_{out} + R_{in})^3}{4r}\right]. \tag{3.9}$$

Midway between the outer and inner boundaries of the annulus, this zonal flow has the same values of $\hat{\sigma}$ and $\hat{v}_\phi$ (zero) as the zonal flow used in figure 1. We found that all of the qualitative features of the family of vortices in §3.7 were shared by the families of vortices produced in this zonal flow. We speculate that any zonal flow in which $\hat{\sigma}(r)$ does not change sign and does not change in magnitude over lengthscales smaller than the size of the vortices also shares these properties. Of course if $\hat{\sigma}(r)$ does change sign, the dynamics can be strikingly different as shown in the next section and by Marcus (1988).

3.9. *Behaviour when $\hat{\sigma}(r)$ changes sign*

In §3.2 we showed that large vortices move according to the sign of $\langle\hat{\sigma}\rangle/\langle\omega\rangle$; when $\langle\hat{\sigma}\rangle/\langle\omega\rangle < 0$, the vorticity is drawn into a spiral and pushed to the radial boundaries; when $\langle\hat{\sigma}\rangle/\langle\omega\rangle > 0$, the vorticity is focused approximately midway between the radial boundaries. By examining vortex dynamics in a zonal flow in which $\hat{\sigma}(r)$ changes sign, we now show that this movement depends upon the *local* sign of $\hat{\sigma}(r)/\langle\omega\rangle$, where $\langle\omega\rangle$ is defined as before and $\hat{\sigma}(r)$ is the value of the zonal shear at the vortex's current location and which changes in time as the vortex moves. We use the zonal flow

$$\hat{v}_\phi = -\tfrac{1}{6}r^2\left[2 + \left(\frac{R_{in} + R_{out}}{2r}\right)^3\right], \tag{3.10}$$

which has

$$\hat{\sigma}(r) = \tfrac{1}{3}r\left[\left(\frac{R_{in} + R_{out}}{2r}\right)^3 - 1\right]. \tag{3.11}$$

The bottom topography is $h(r) = -(r - \tfrac{5}{6})$. The zonal flow has two distinct bands. The inner band with $R_{in} \leqslant r < \tfrac{1}{2}(R_{in} + R_{out})$ has $\hat{\sigma}(r) > 0$; the outer with $\tfrac{1}{2}(R_{in} + R_{out}) \leqslant r \leqslant R_{out}$ has $\hat{\sigma}(r) < 0$. The initial ω is shown in figure 7(*a*) (plate 4) and consists of two vortices in each band – one counterclockwise (red) and one clockwise (blue). The red vortex in the outer band and the blue vortex in the inner have $\hat{\sigma}(r)/\langle\omega\rangle < 0$, and figure 7(*b*) shows that both are stretched into spirals with ends drawn to the boundaries of the band – either the boundary of the annulus or the boundary between the bands at $r = \tfrac{1}{2}(R_{in} + R_{out})$. The blue vortex in the outer band and the red vortex in the inner, both with $\hat{\sigma}(r)/\langle\omega\rangle > 0$, remain almost unchanged. As the leading edges of the spirals with $\hat{\sigma}(r)/\langle\omega\rangle < 0$ pass between the two bands, the ω rolls up to form two small clumps at the end of each spiral (figure 7*b*, *c*). Once these small clumps of ω have passed from one band into the other, they are in background shears with $\hat{\sigma}(r)/\langle\omega\rangle > 0$. The clumps then detach from their respective spirals and form stable vortices (figure 7*d*). The remaining pieces of the two spirals that do not cross-over into the neighbouring band fragment and end as filaments of ω dispersed throughout their respective bands. After a few more turn-around times each of the two small surviving vortices in figure 7(*d*) merges with its neighbouring large vortex.

The size of the clumps of vorticity that pass across the $r = \tfrac{1}{2}(R_{in} + R_{out})$ boundary into the neighbouring band and survive as coherent vortices depends crucially on their initial locations. In particular, it depends on the difference between the

timescale for the leading edge of a spiral to cross into the neighbouring band and either the timescale for the linear instability to grow to finite amplitude and fragment it or the timescale for the thin spiral to dissipate. For example, increasing the distance between the initial locations of the four vortices in figure 7(a) and the $r = \frac{1}{2}(R_{in} + R_{out})$ boundary by only 10 % prevents the leading edges of the spirals from reaching the boundary before the spirals fragment, and no coherent clumps of vorticity pass into the neighbouring bands.

Marcus (1988) examined a zonal flow with sinusoidal $h(r)$ and $\hat{v}_\phi(r)$ such that there were four concentric annular bands with the sign of $\hat{\sigma}(r)$ changing between each band and found that with four bands as well as two, all large vortices with $\hat{\sigma}(r)/\langle \omega \rangle < 0$ either fragment or are pushed to a neighbouring band where they are stable. Thus we conclude that in a zonal flow in which $\hat{\sigma}(r)$ changes sign, it is the *local* instantaneous sign of $\hat{\sigma}(r)/\langle \omega \rangle$ that determines the vortex behaviour.

4. Unstable vortex layers in shear flows

4.1. *Early evolution – linear behaviour*

The breakup of a vortex layer has been studied by a number of authors (cf. Dritschel 1985). Here, we examine the breakup of vortex layers and their late-time behaviour when they are embedded in zonal flows. Our motivation is not that we are interested in the behaviour of vortex layers *per se*, but that their behaviour is illustrative of much of the dynamics of vortices in a zonal flow, and they provide an analytically tractable example of how the exchange between the interaction energy and self-energy affects vortices. In particular, we shall show that whether the layer breaks up to eventually form one large vortex or successively smaller filaments depends on whether the self-energy increases or decreases, which in turn depends on the sign of $\hat{\sigma}/\omega$.

We begin by examining a flow that initially consists of the superposition of a shearing zonal flow

$$\hat{v}_\phi = \tfrac{1}{6}r(2r - R_{in} - R_{out}) \tag{4.1}$$

and an axisymmetric vortex layer with vorticity

$$\omega = \frac{0.833}{r} \operatorname{sech}^2[10(r - 0.833)] + \omega_0 \tag{4.2}$$

and velocity

$$v_\phi = \frac{0.0833}{r}\{\tanh[10(r - 0.833)] - \tanh[10(R_{in} - 0.833)]\} + \tfrac{1}{2}\omega_0\left(r - \frac{R_{in}^2}{r}\right), \tag{4.3}$$

$$v_r = 0. \tag{4.4}$$

As in §3, $h(r) = (r - \frac{5}{6})$ and $R_{in}/R_{out} = 0.25$. (The value of ω_0 in (4.3) and (4.4) is chosen to be consistent with the definitions of C_1 and C_2 in §2.2.) The vortex layer is centred midway between the inner and outer radial boundaries, has radial thickness of approximately 0.2, and an ω that is approximately uniform throughout the layer with a value of unity, so in the layer $\hat{\sigma}/\omega \approx 0.28$. Note that $\hat{\sigma}/\omega > 0$ throughout the entire flow. The initial ω is shown in figure 8(a) (plate 5). Because the vortex layer is axisymmetric it is a steady-state solution to the equations of motion and has no linearly unstable axisymmetric perturbations. Because our computational method preserves the symmetries in the round-off errors, the vortex layer in figure 8(a) is also

a stable equilibrium solution of our initial-value code. To examine non-axisymmetric instabilities we add a small random component to the initial flow with an energy that is 10^{-10} of the energy of the axisymmetric component of the vortex layer and is so small that it is not visible in figure 8(*a*). This new flow is linearly unstable, and its subsequent evolution is shown in figure 8(*b–h*) (plates 5, 6). Not surprisingly, the early time evolution is dominated by the most unstable eigenmodes of the vortex layer. We have numerically computed these eigenmodes and their eigenvalues and found that they are similar to those of a model vortex layer that has uniform strength with $\omega \equiv 1$ for $(0.833-0.1) \equiv \bar{R}_1 \leqslant r \leqslant \bar{R}_2 \equiv (0.833+0.1)$ and $\omega \equiv 0$ outside this annular strip. The advantage of studying the model vortex layer is that although the vorticity is discontinuous, the linear and weakly nonlinear dynamics can be computed analytically in closed form. The fastest growing eigenmodes of both the actual and the model vortex layer are of the form $e^{i3\phi}$ and have their greatest amplitudes at the outer edge of the layer. This is shown in the fully nonlinear solution in figure 8(*b*) at $t = 3.34$ (in turn-around time units based on $\omega = 1$). The fact that amplitude is greater at the outer edge is due to the curvature of the vortex layer and not due to $\hat{v}_\phi(r)$ or $h(r)$; it is shown in the Appendix that, as the curvature goes to zero, the amplitudes at the two edges become equal regardless of the functional form of $\hat{v}_\phi(r)$ and $h(r)$. The fact that the fastest growing wavenumber in figure 8(*b*) is small is because the azimuthal wavenumber m of the fastest growing eigenmode of an unbounded, annular, vortex layer with uniform strength ω is

$$m = \left(\frac{2}{1-\gamma^2}\right)\left(\frac{\omega}{\omega+\langle\hat{\sigma}\rangle}\right)\left[1+\left(\frac{2}{1-\gamma^2}\right)\left(\frac{\omega}{\omega+\langle\hat{\sigma}\rangle}\right)\gamma^{2m}\ln(\gamma)\right], \qquad (4.5)$$

where we define the characteristic shear of the zonal flow at the layer as

$$\langle\hat{\sigma}\rangle \equiv \frac{2}{1-\gamma^2}\left(\frac{\hat{v}_\phi(\bar{R}_2)}{\bar{R}_2}-\frac{\hat{v}_\phi(\bar{R}_1)}{\bar{R}_1}\right) \qquad (4.6)$$

and $\gamma \equiv \bar{R}_1/\bar{R}_2$. For thin vortex layers, i.e. $\gamma \to 1$, $\langle\hat{\sigma}\rangle$ approaches the value of $\hat{\sigma}(r)$ at the vortex layer. For $\langle\hat{\sigma}\rangle/\omega > -1$, equation (4.5) shows that the fastest growing wavenumber m increases with decreasing $\langle\hat{\sigma}\rangle/\omega$. For $0 > \langle\hat{\sigma}\rangle/\omega > -1$, m increases very rapidly as $\langle\hat{\sigma}\rangle/\omega$ decreases and becomes infinite as $\langle\hat{\sigma}\rangle/\omega \to -1$. For $\langle\hat{\sigma}\rangle/\omega < -1$, the flow is linearly stable. (See figure 9 and the Appendix.) Equation (4.5) agrees very well with our numerical calculations of the eigenmodes of the continuous vortex layer in (4.2) and with the solutions of the initial-value code. The phase speed of the eigenmode of the model vortex layer is $\frac{1}{2}[(u_\phi(\bar{R}_1)/\bar{R}_1)+(u_\phi(\bar{R}_2)/\bar{R}_2)]$, and we have found that this is the approximate phase speed of the eigenmode of the actual layer and is approximately equal to the pattern speed in figure 8(*b*).

4.2. *Weakly nonlinear growth*

Much of the subsequent evolution of the breakup of the vortex layer can be understood by a finite-amplitude expansion and the use of the conservation laws. Let the model vortex layer be initially perturbed by its most unstable eigenmode with amplitude ϵ and wavenumber m. The locations of the two edges of the vortex layer are then

$$R_1(t,\phi) = \bar{R}_1 + \epsilon^2 A_0(t) + \epsilon A_1(t)\,e^{im\phi} + \epsilon^2 A_2(t)\,e^{2im\phi} + O(\epsilon^3), \qquad (4.7)$$

$$R_2(t\,\phi) = \bar{R}_2 + \epsilon^2 B_0(t) + \epsilon B_1(t)\,e^{im\phi} + \epsilon^2 B_2(t)\,e^{2im\phi} + O(\epsilon^3), \qquad (4.8)$$
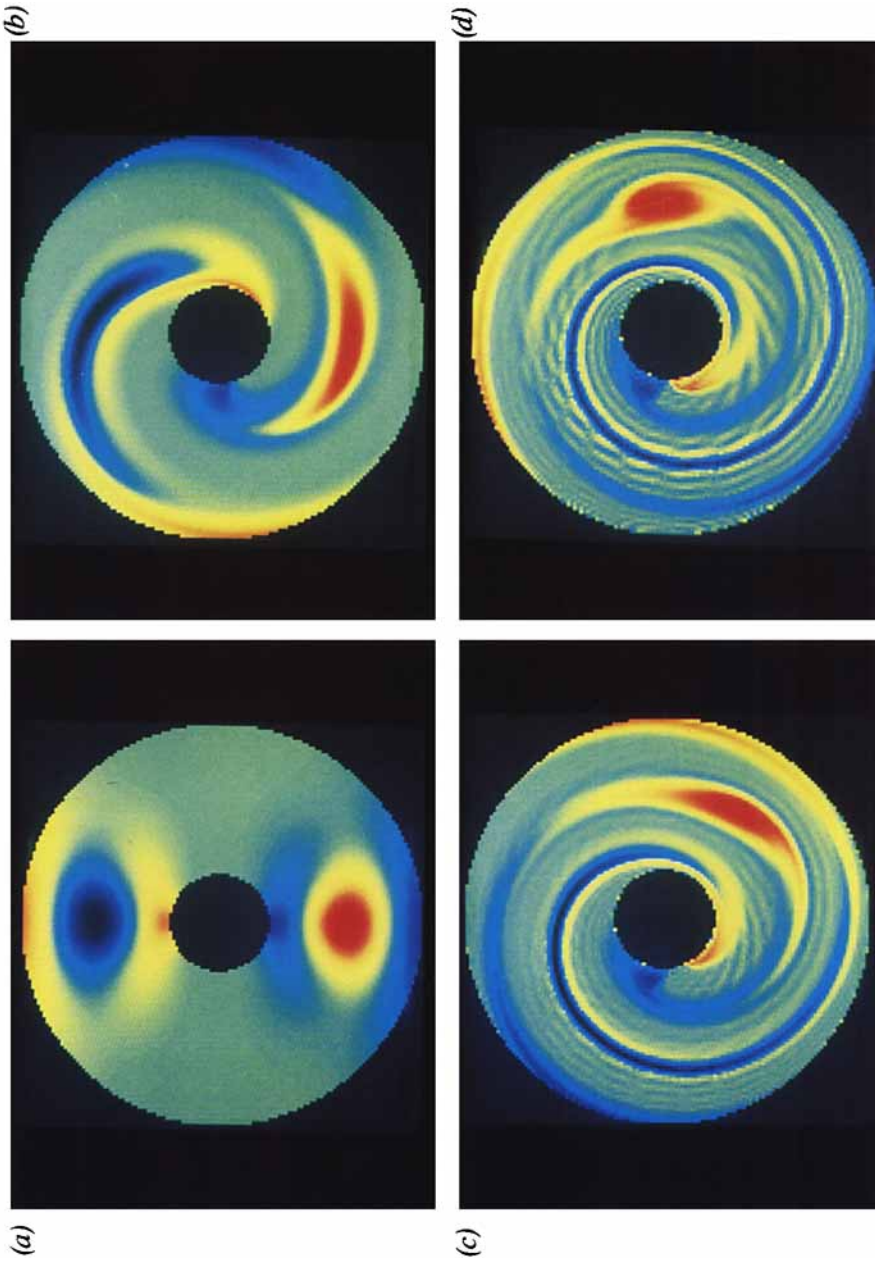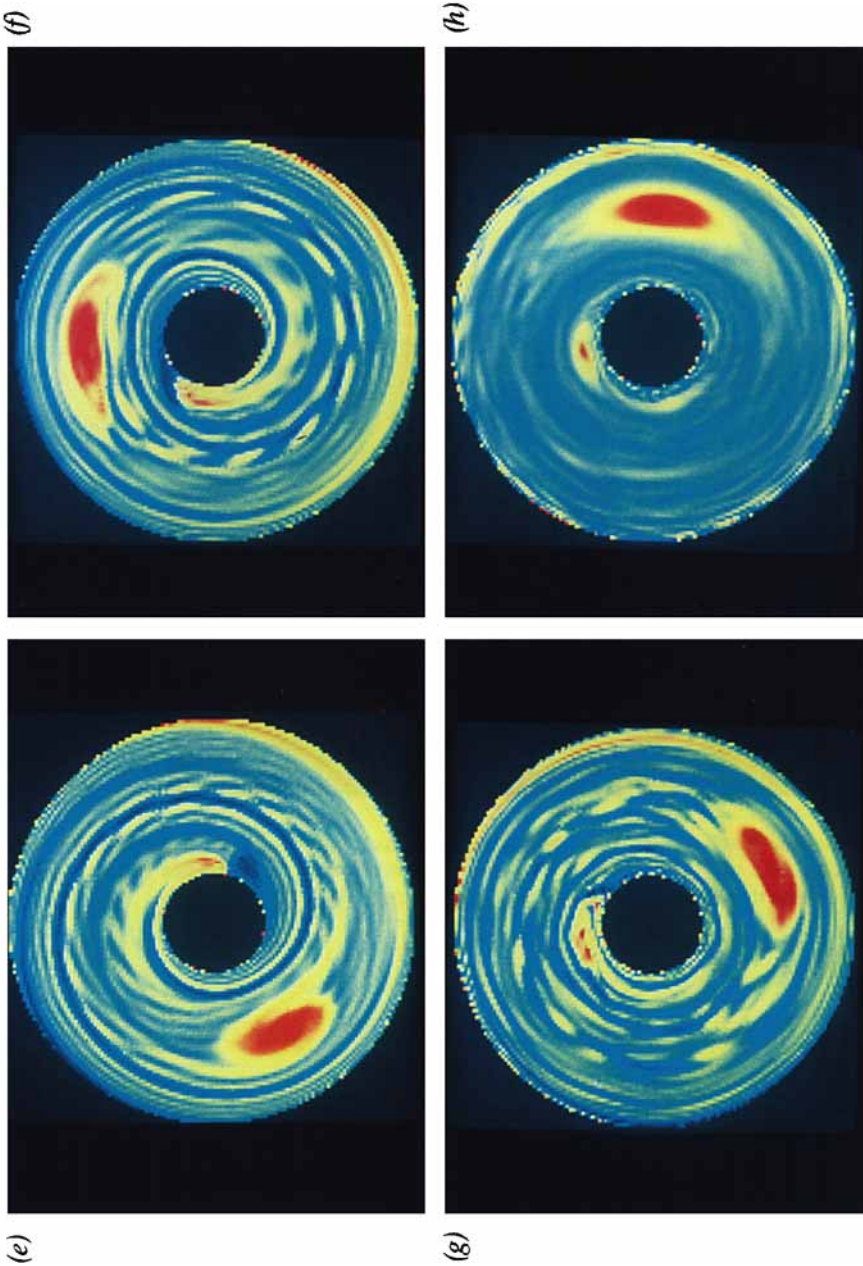
FIGURE 1. Evolution of flow with $\hat{v}_\phi$ and stream function given by equations (3.1) and (3.2). The angular velocity of the zonal flow increases linearly with r; it is clockwise at R_{in}, counterclockwise at R_{out}, and zero at $\frac{1}{2}(R_{in} + R_{out})$. At the centre of each large vortex $\delta/\omega = O(1)$. $(a - h)$ Correspond to the flow after 0, 0.298, 0.648, 0.863, 1.01, 1.29, 6.04, and 20.7 turn-around times. Each figure has only 64×64 independent pixels, whereas the numerical calculation was done with 256×128 Chebyshev-Fourier modes. The low pixel resolution makes a green background filled with thin blue filaments appear uniformly turquoise. Note that because the computations were done in a constantly changing reference frame (to minimize the Courant number) the azimuthal orientation of each figure is arbitrary.
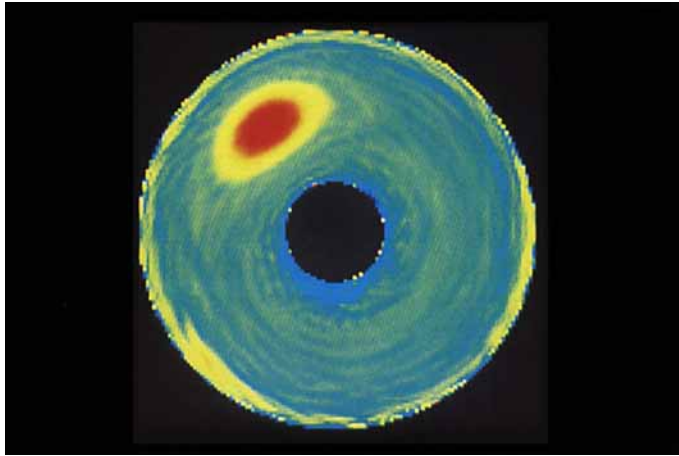
FIGURE 4. The ω of a flow that initially looks like that in figure 1(a), but with $\hat{\sigma}/\omega$ one third the strength. The flow is shown after 62.1 turn-around times. The vortex is much rounder than the one shown in figure 1(h) and it has swallowed the smaller vortex that was initially near R_{in}.
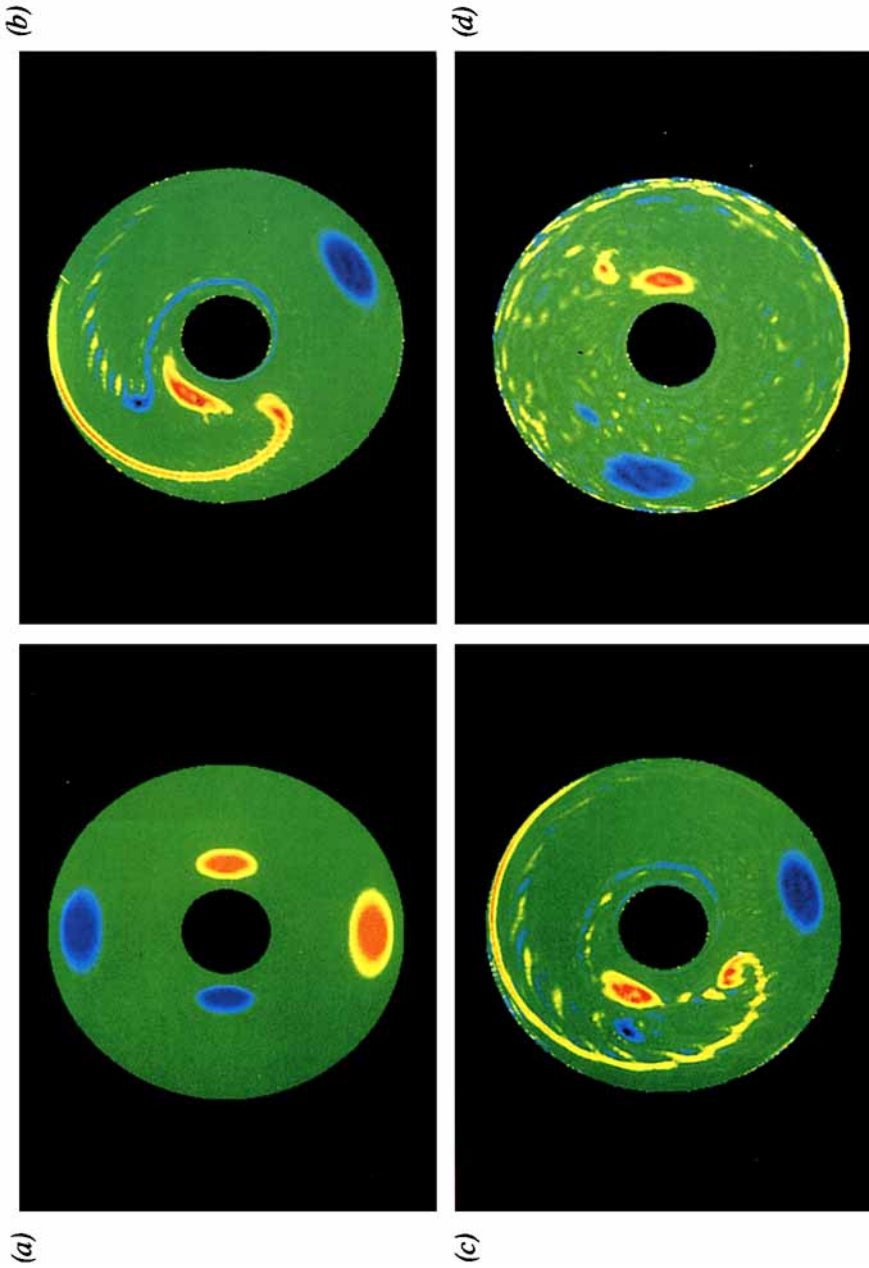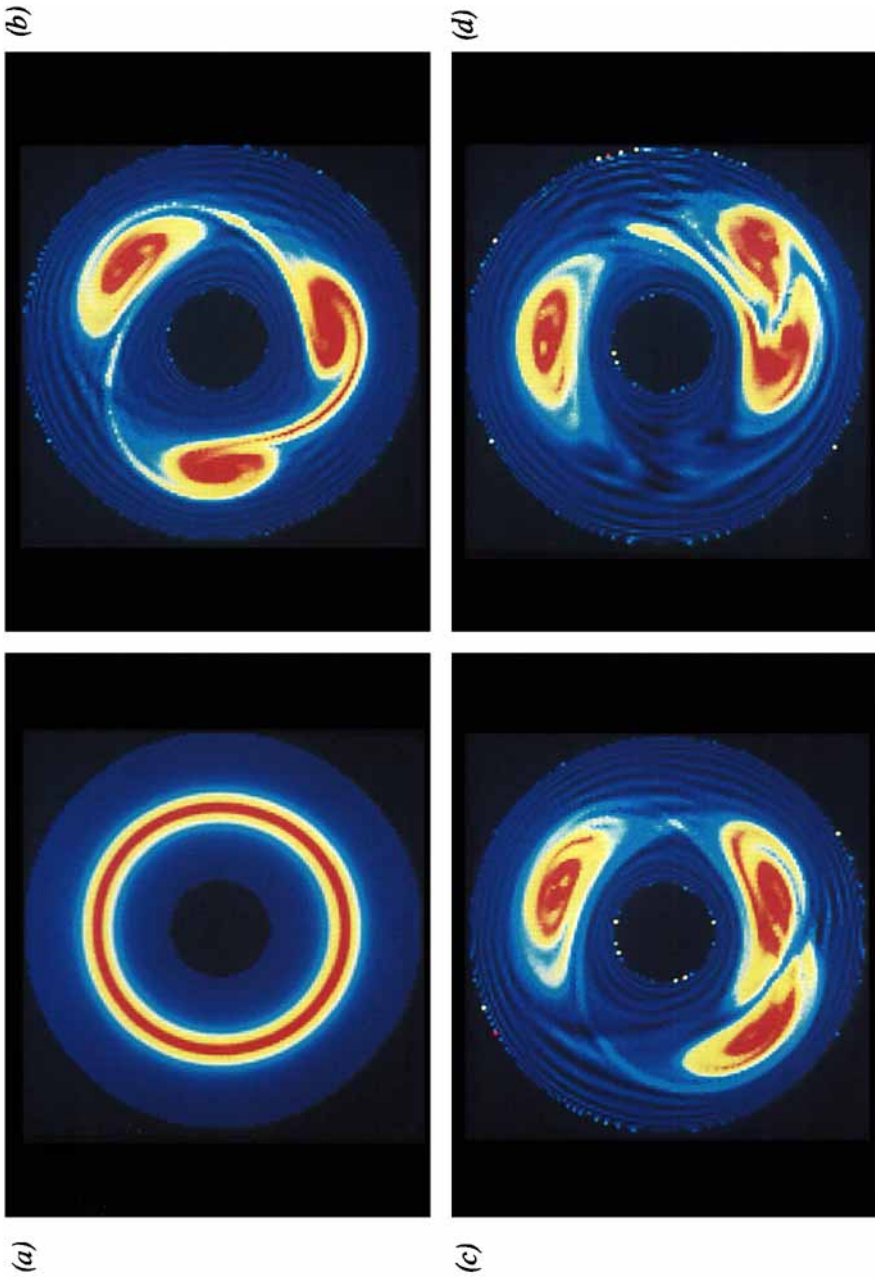
FIGURE 7. Vortices in a zonal flow given by equation (3.10) with two bands where $\hat{\sigma}(r) < 0$ in the outer band of the annulus and $\hat{\sigma}(r) > 0$ in the inner band. The angular velocity of the zonal flow is everywhere clockwise but has its smallest absolute value at $\frac{1}{2}(R_{in} + R_{out})$. Counterclockwise (red) vortices are stable in the inner half and ejected from the outer half.
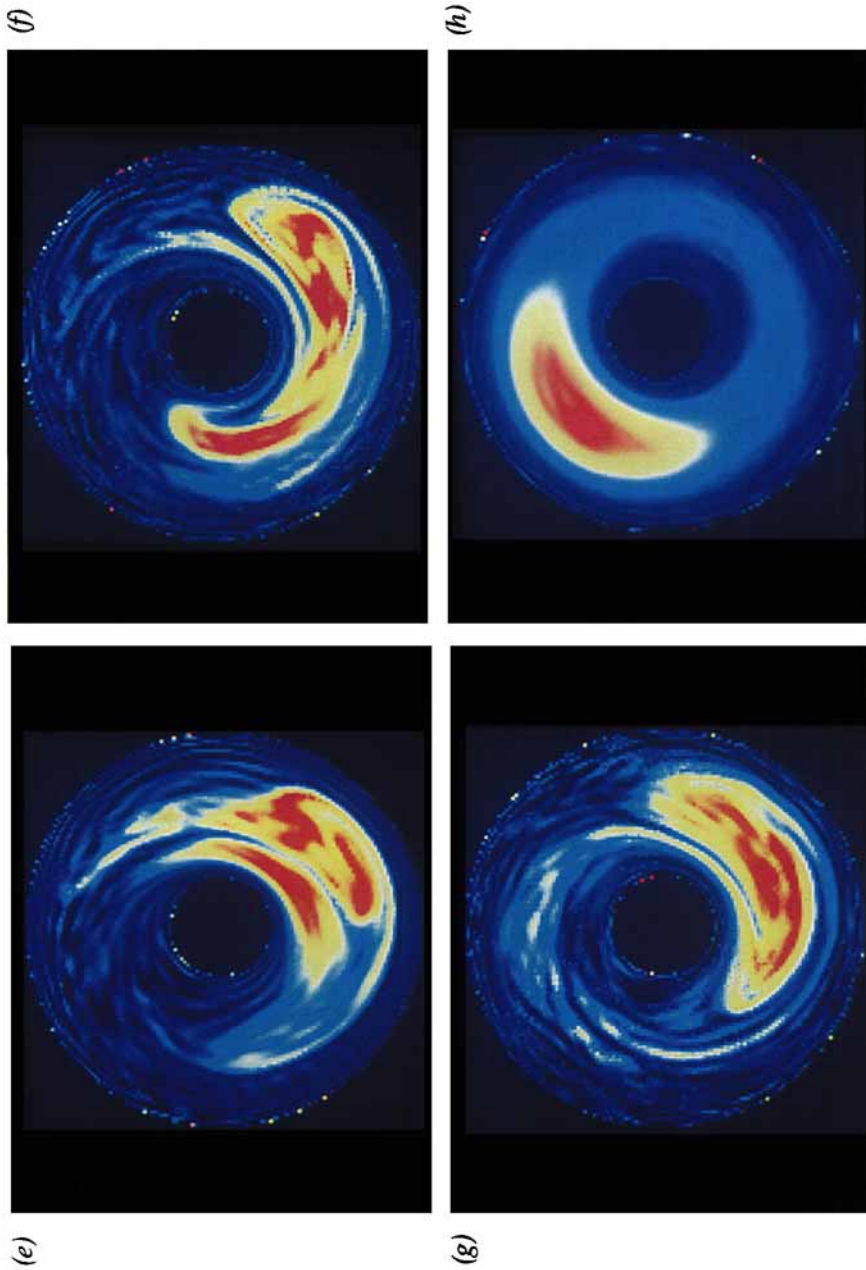
FIGURE 8. Evolution of the ω of a linearly unstable shear layer with $\delta/\omega = 0.28$ and with the same zonal velocity as in figure 1. The layer breaks up into a three-fold symmetric eigenmode (the most rapidly growing one). The three vortices separate from each other, merge together, and eject the irrotational (light blue and yellow) fluid entrained near the vortex centre. (*a - h*) After 0, 3.34, 3.82, 4.46, 5.73, 6.21, 7.64, and 29.6 turn-around times.
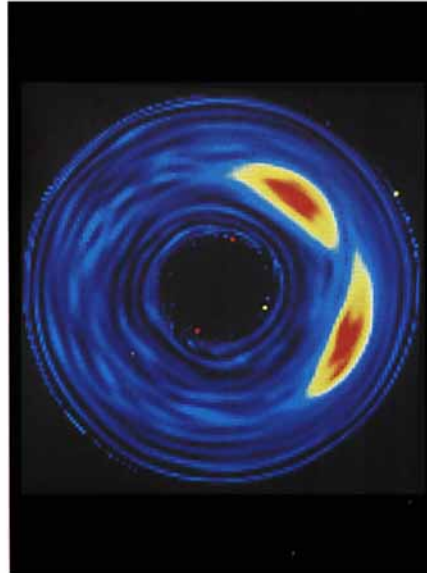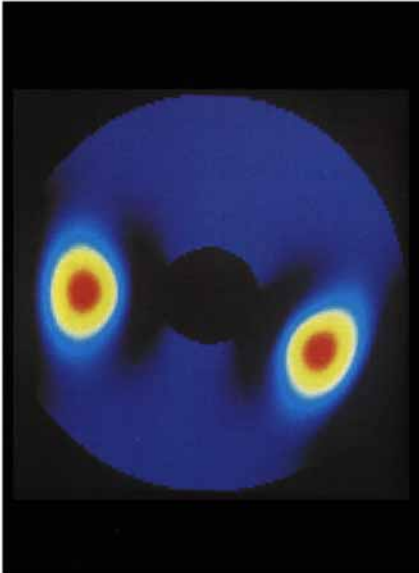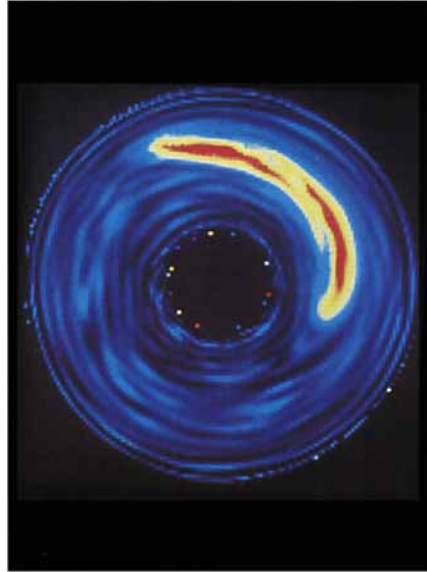
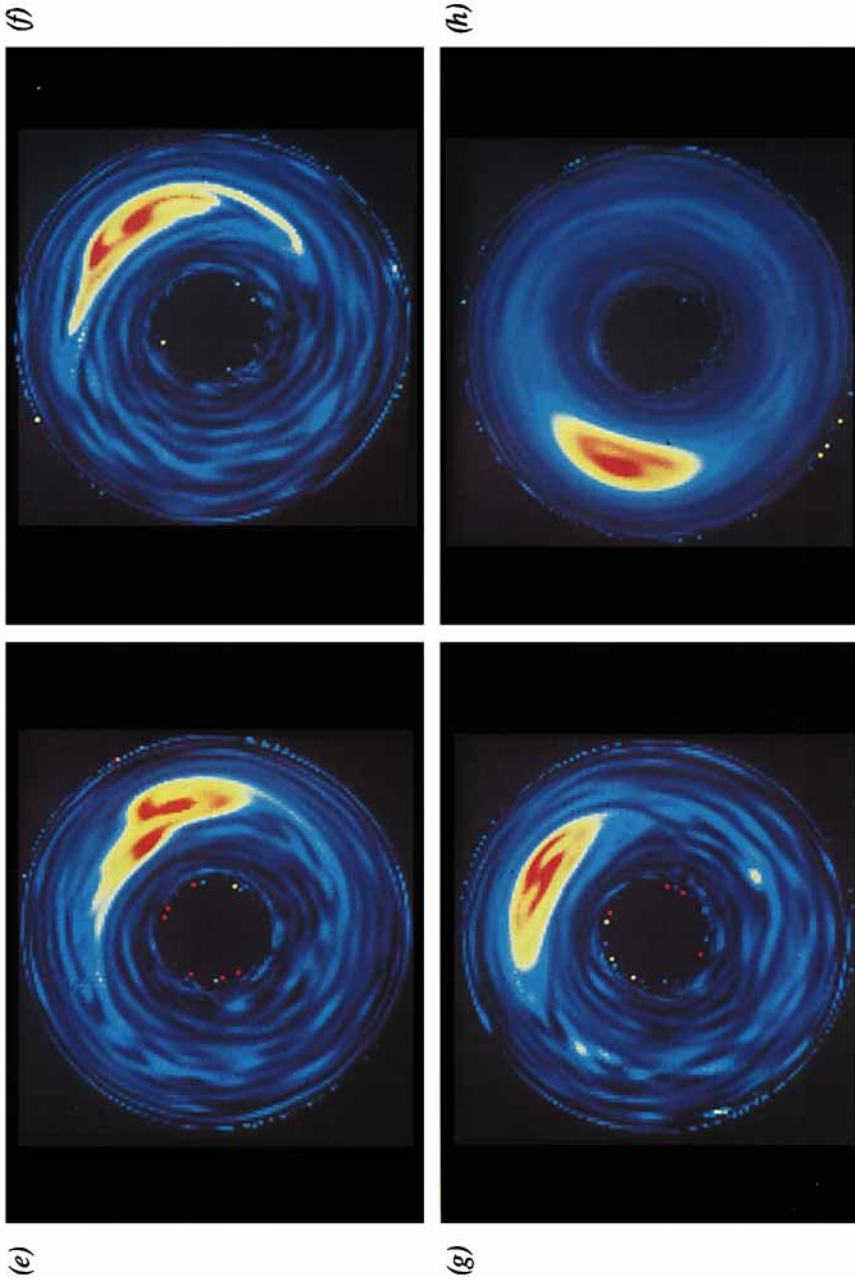FIGURE 10. Evolution of ω starting with two vortices with $\delta/\omega = O(1)$, with the same $\bar{\psi}$ as in figure 1, and with $\Delta r = 0$. $(a - h)$ Correspond to the flow after 0, 1.29, 3.45, 4.31, 5.17, 6.04, 6.90, and 26.7 turn-around times.
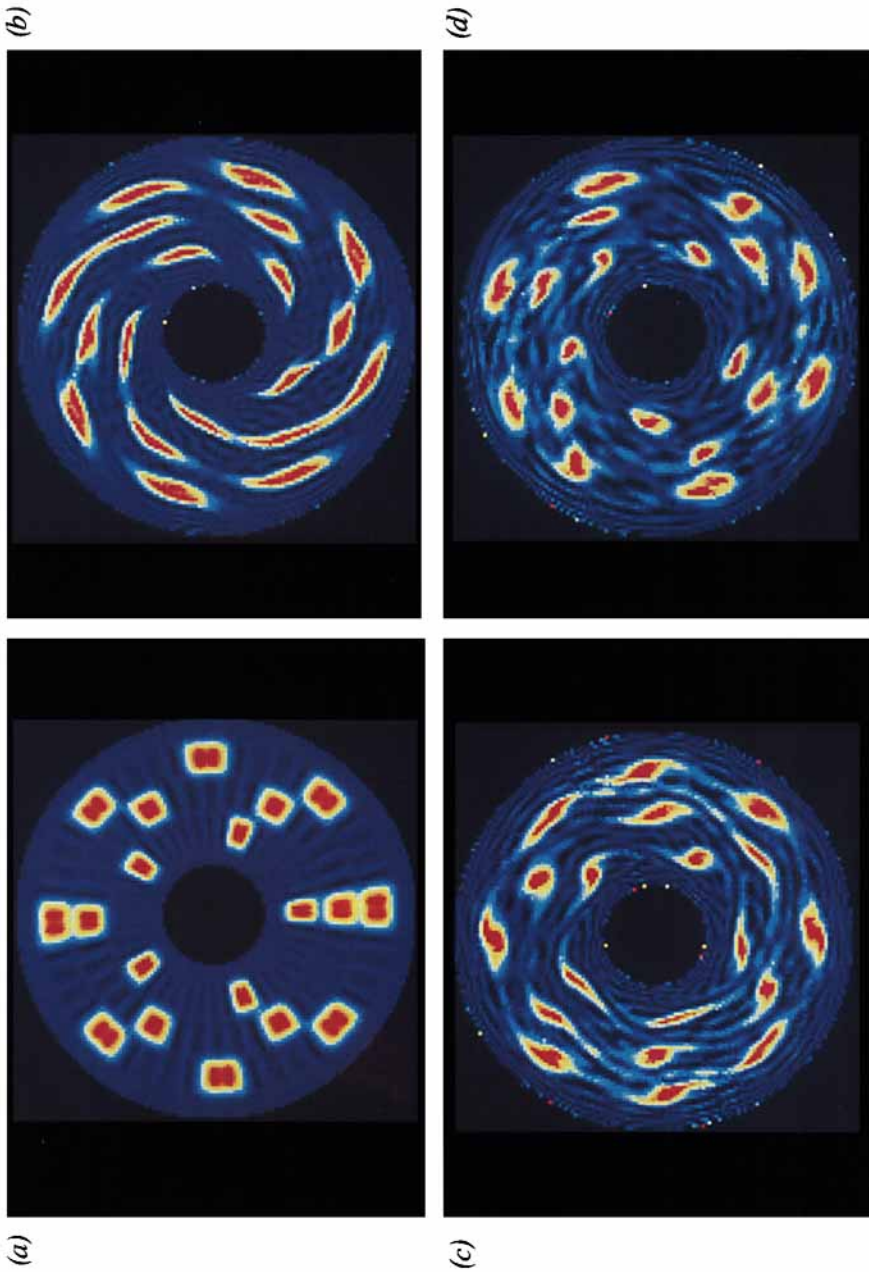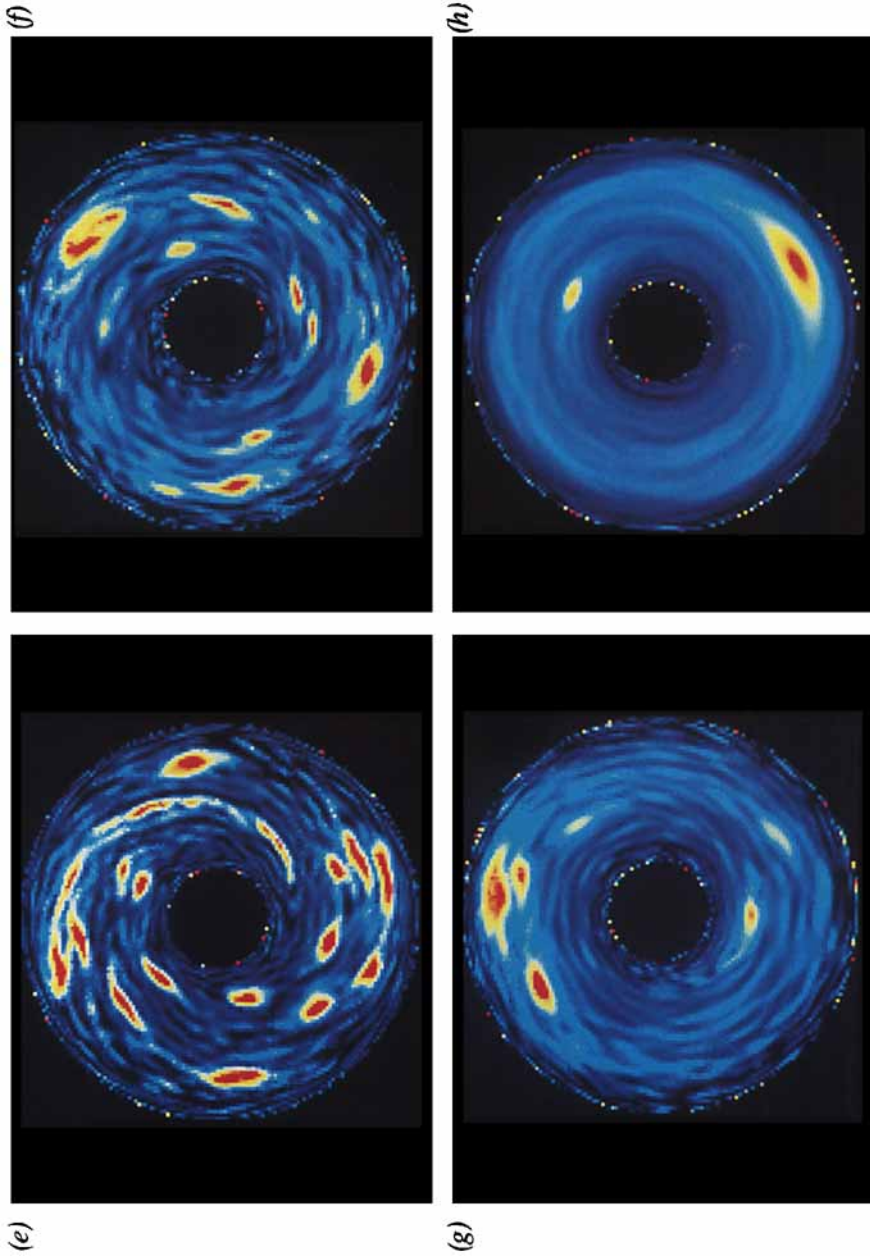
FIGURE 11. Evolution of ω initially with a checkerboard pattern of vortices with $\omega \approx 0.424$, and with the same $\hat{v}$ as in figure 1 and $\hat{\sigma}/\omega > 0$. There is a large amount of dissipation of enstrophy (and destruction of red pixels) due to the filamentation caused by the vortex collisions transferring enstrophy directly from the large scales to the small, dissipative scales. $(a - h)$ Correspond to the flow after 0, 0.346, 1.04, 1.38, 4.31, 15.5, 34.9 and 51.7 turn-around times.

FIGURE 9. The unstable wavenumbers α of a planar vortex layer of strength ω embedded in a planar zonal flow with shear $\langle \hat{\sigma} \rangle$. The fastest growing mode for fixed $(\langle \hat{\sigma} \rangle + \omega)/\omega$ is shown by the long-dashed curve. The dotted curve is $\alpha = \omega/(\langle \hat{\sigma} \rangle + \omega)$. The two solid curves and the long-dashed curve all approach the dotted curve as $(\langle \hat{\sigma} \rangle + \omega)/\omega \to 0$.
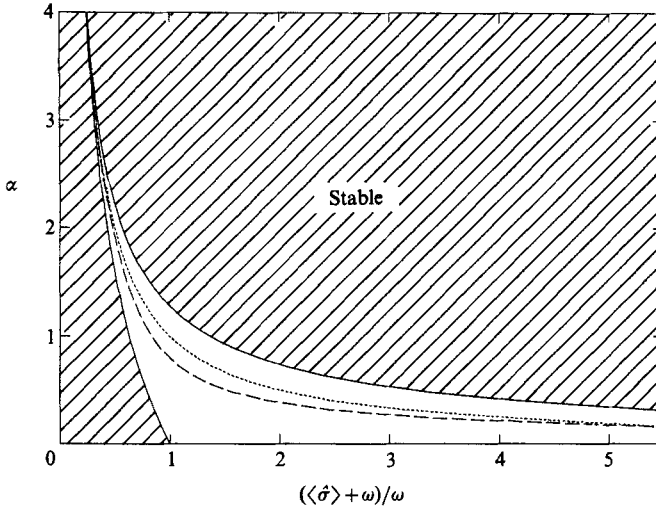
with $A_0(0) = B_0(0) = A_2(0) = B_2(0)$, and $A_1(0)$ and $B_1(0)$ equal to the coefficients of the normalized, most-unstable, eigenmode (given in the Appendix). Conservation of the two independent circulations requires that

$$\int_0^{2\pi} \mathrm{d}\phi \int_0^{R_1(t,\,\phi)} r\,\mathrm{d}r \quad \text{and} \quad \int_0^{2\pi} \mathrm{d}\phi \int_0^{R_2(t,\,\phi)} r\,\mathrm{d}r$$

are time-independent, or equivalently

$$A_0(t) = -\frac{1}{4\bar{R}_1}[|A_1(t)|^2 - |A_1(0)|^2] + O(\epsilon^2), \tag{4.9}$$

$$B_0(t) = -\frac{1}{4\bar{R}_2}[|B_1(t)|^2 - |B_1(0)|^2] + O(\epsilon^2). \tag{4.10}$$

Because $|A_1(t)|^2$ and $|B_1(t)|^2$ increase approximately exponentially at early times, $A_0(t)$ and $B_0(t)$ decrease exponentially at early times, and the vortex layer moves radially inward. This behaviour is observed in the flow in figure 8. Note that this behaviour is independent of the functional forms of $h(r)$ and $\hat{v}_\phi(r)$ and so is also true for annuli with flat bottom boundaries and for flows with $\hat{v}_\phi \equiv 0$.

Conservation of angular momentum requires that

$$\int_0^{2\pi} \mathrm{d}\phi \int_{R_1(t,\,\phi)}^{R_2(t,\,\phi)} r^3\,\mathrm{d}r$$

is time-independent, or equivalently

$$[|B_1(t)|^2 - |B_1(0)|^2] = (\bar{R}_1/\bar{R}_2)^2[|A_1(t)|^2 - |A_1(0)|^2] + O(\epsilon^2). \tag{4.11}$$

Equation (4.11) shows that the growth of the perturbation at the outer side of the vortex layer is slower than the growth at the inner side, regardless of the values of

$\hat{v}_\phi$ and $h(r)$. This is illustrated in figure 8; although the perturbation is initially larger at the outside edge of the layer, the asymmetry of the edges decreases in time.

The conservation of energy and the exchange between the vortex layer's self-energy and the interaction energy are particularly useful in understanding the weakly nonlinear behaviour. The change in the interaction energy of a model vortex layer embedded in a zonal flow is (using the definition in (2.20))

$$E^{\mathrm{int}}(t) - E^{\mathrm{int}}(0) \equiv -\int_D [\omega(r,t) - \omega(r,0)]\,\hat{\psi}(r)\, r\, \mathrm{d}r\, \mathrm{d}\phi$$

$$= -\frac{\pi\epsilon^2 \bar{R}_1^2(\bar{R}_2^2 - \bar{R}_1^2)}{4\bar{R}_2^2} \langle \hat{\sigma} \rangle\, \omega[|A_1(t)|^2 - |A_1(0)|^2] + O(\epsilon^4). \quad (4.12)$$

To obtain (4.12) we used (4.4)–(4.11), the definition of $\langle \hat{\sigma} \rangle$ in (4.6), and carried out a Taylor expansion of $\int^{r(\phi,t)} \hat{\psi}(r)\, r\, \mathrm{d}r\, \mathrm{d}\phi$ about $r = \bar{R}_1$ and $r = \bar{R}_2$. Equation (4.12) shows that the change in E^{int} is independent of the detailed functional form of $\hat{v}_\phi(r)$ and depends only on the value of $\langle \hat{\sigma} \rangle$ as defined in (4.6). For $\langle \hat{\sigma} \rangle/\omega > 0$ (as in the flow in figure 8), when $[|A_1(t)|^2 - |A_1(0)|^2]$ increases in time, $E^{\mathrm{int}}(t)$ decreases. Because the total energy is conserved, $E^{\mathrm{self}}(t)$ must increase. The hallmark of a flow with increasing E^{self} is that it evolves from its initial conditions into one in which the spatial distribution of ω becomes more compact. The formation of the three vortices and their subsequent merger shown in figure 8 is consistent with this picture, and we have found numerically that E^{int} decreases monotonically throughout the entire evolution. Equation (4.12) also shows that for an unstable flow, when

$$-1 < \langle \hat{\sigma} \rangle/\omega < 0,$$

E^{int} increases, and E^{self} decreases in time. The hallmark of a flow with decreasing E^{self} is that the distribution of ω becomes dispersed. Our numerical simulation of the initial flow in figure 8(a) with ω replaced with $-\omega$ and with the same zonal flow as in figure 8 shows the vortex layer is unstable with respect to small-wavelength eigenmodes as predicted by (4.5). The layer breaks into thin filaments that become dispersed throughout the annulus. No large vortices form, and E^{self} decreases monotonically throughout the evolution. In summary, the vortex layer's behaviour depends on whether E^{self} decreases or increases in time, which in turn depends on the signs of $\langle \hat{\sigma} \rangle/\omega$ and $\mathrm{d}A_1/\mathrm{d}t$. For $\langle \hat{\sigma} \rangle/\omega > 0$, the layer is unstable, so $\mathrm{d}A_1/\mathrm{d}t > 0$ and E^{self} increases; for $0 > \langle \hat{\sigma} \rangle/\omega > -1$, the layer is unstable, so $\mathrm{d}A_1/\mathrm{d}t > 0$ but E^{self} decreases; and for $-1 > \langle \hat{\sigma} \rangle/\omega$, the layer is neutrally stable, so an initially perturbed layer has $\mathrm{d}A_1/\mathrm{d}t = 0$ with E^{self} constant.

4.3. *Nonlinear behaviour – expulsion of weakly rotating fluid and merger*

The full details of the late-time flow, of course, cannot be determined from (4.12) alone. Our numerical simulation shows that the three vortices in figure 8(b) separate from each other (owing to the small amount of numerical dissipation and diffusion) and then merge together. The resulting large vortex in figure 8(h) is distorted from an ellipse into a 'croissant' shape by the proximity of the annular boundaries. The vortex is large because the initial red vortex layer has a large area and this area is conserved when there is no dissipation. During the merger of the three red vortices some ω is shed filaments. Most of the red and orange filaments reattach quickly. Some of the yellow reattaches, but much does not, and it migrates to the boundary layers or ends up dispersed in the zonal component of the flow. The filaments make

the resulting zonal component of the flow temporally chaotic, and although the potential vorticity of the macroscopic zonal flow remains uniform, there are large fluctuations in it on the lengthscale of the filaments. Most of the vorticity that goes into the filaments is shed from the large vortices during the violent collisions between $t = 3.5$ and $t = 8$. The area of the large vortex in figure 8(g) that lies within the isovorticity contour with $\omega = 0.8$ is 93% of the area of the initial flow in figure 1(a) with $\omega \geqslant 0.8$. Less than 1% of this circulation is lost through dissipation; most goes into the shed filaments. From $t = 0$ to $t = 8$ the total energy of the flow decreases by less than 0.1% owing to dissipation. However, the energy of the flow inside the $\omega = 0.8$ isovorticity contour of the large vortex decreases by 8%. This energy is transferred to the filaments dispersed throughout the zonal flow. It is this energy transfer from the large vortex to the filaments that allows the large vortex to relax to its equilibrium state in a timescale that is fast compared to the dissipative one.

As the vortices in figure 8 merge together, they initially sandwich a lot of less rapidly rotating, yellow, ω between them (shown at the bottom of figures 8$d-f$). Most of this less rapidly rotating fluid is ejected to the outside of the two merging vortices on the fast, advective timescale before it is completely encircled by isovorticity contours with large ω. However, some less rapidly rotating (yellow) fluid with $\omega \approx 0.4$ does get trapped and surrounded by isovorticity contours with $\omega \approx 0.8$. If the flow were dissipationless, it would be impossible for this yellow fluid to pass across these isovorticity contours and escape the vortex. Our calculations show that in a few turn-around times most of the yellow $\omega \approx 0.4$ fluid is pushed from the vortex centre to the periphery but not outside the $\omega \approx 0.8$ contours. Once at the periphery, the yellow fluid remains there as a compact region and orbits around the centre of the vortex with the velocity of the surrounding fluid. Only on a long, dissipative time does the entrapped fluid with $\omega \approx 0.4$ break up or dissipate. Approximately half of it is spun up by the surrounding fluid and loses its identity by increasing its ω (turning from yellow to red). The other half leaks to the outside of the large red vortex and remains attached there. (This is determined numerically by following particle paths.) Most, but not all, of the less rotational yellow fluid is gone from the interior of the final vortex in figure 8.

Thus, to fully understand the merging of the vortices in figure 8, it is necessary to understand how a vortex with a local minimum of $|\omega|$ at its centre expels the less rapidly rotating fluid. Inviscid linear theory can be used to calculate the unstable eigenmodes of a zonal flow superposed with a model vortex with a local minimum of $|\omega|$ at its centre (see the Appendix); however, the mechanics of how the instability turns the vortex 'inside out' so that the less rapidly rotating fluid is on the outside can only be determined from a numerical calculation with dissipation. Therefore we have examined numerically a one-parameter family of flows whose initial states consist of a vortex with strength unity nested inside and concentric with another vortex of strength $(1+\chi)$. The nested vortices are superposed on the zonal flow in equation (4.1) such that their centres are located at $r = \frac{1}{2}(R_{\mathrm{in}}+R_{\mathrm{out}})$. The two nested vortices both have ellipticity equal to two. Their major axes are both aligned in the azimuthal direction. Specifically, the value of ω of the initial flow is

$$\omega = [1+\tfrac{1}{2}\chi(1+\tanh\{60[(x^2+4y^2)^{\frac{1}{2}}-0.16]\})]\tfrac{1}{2}(1-\tanh\{60[(x^2+4y^2)^{\frac{1}{2}}-0.32]\})], \tag{4.13}$$

where x and y are the local Cartesian coordinates with origin at the centre of the vortices and x-axis aligned with the azimuthal direction. The value of ω is constant along concentric elliptical contours with ellipticity of two. The semi-major axes of

the inner and outer nested vortices are 0.16 and 0.32, respectively. For $\chi < 0$, the ω of the vortex decreases from the centre to the edge, and our numerical calculations show that the vortex relaxes to its equilibrium without expelling fluid from its interior. For $\chi > 0$ the fluid at the centre is less rapidly rotating, so there is a local minimum of $|\omega|$ inside the vortex, and we have observed two distinct types of behaviour. For $\chi > 0.1$ the vortex breaks apart violently in less than one turn-around time so that the less rapidly rotating fluid at the centre of the initial vortex is no longer trapped. The fragments of the vortex remerge so that none of the less rapidly rotating fluid remains in the interior, and ω decreases from the centre of the vortex to the periphery. For $0.1 > \chi > 0$ the vortex behaviour is similar to the dynamics exhibited by the three vortices formed from the unstable vortex layer in figure 8: within 3 turn-around times most of the less rapidly rotating fluid with $\omega = 1$ is pushed off-centre but remains as a coherent, compact, roundish blob, that orbits around the vortex centre inside the $\omega = (1+\chi)$ isovorticity contours. After several hundred turn-around times it either dissipates or leaks to the outside of the vortex.

We have repeated all of the numerical calculations of this section with $h(r) = 0$ and $\hat{v}_\phi(r) = 0.0937\,[(4r/(R_{in}+R_{out})^2) - (1/r)]$. This zonal flow is similar to that in equation (4.1) in that they have the same value of $\langle \hat{\sigma} \rangle$ (as defined in (4.6)). At $r = \frac{1}{2}(R_{in}+R_{out})$ they both have $\hat{v}_\phi = 0$ and the same value of $\hat{\sigma}$ to within 3%. The dynamics, and in particular the pictures of the evolution of ω, are qualitatively similar for the two zonal flows; thus, we speculate that the behaviour shown in figure 8 is common to zonal flows in which $\hat{\sigma}(r)$ does not change sign, has the same order-of-magnitude strength as the layer's vorticity, and has variations over lengthscales longer than the layer's thickness.

5. Mergers in shear flows

5.1. *The merger of two vortices*

In the last section we saw an example of vortex merger. Mergers are common in our initial-value experiments, and in some ways resemble the mergers of isolated vortices observed by Overman & Zabusky (1982) and Dritschel (1985) in flows without zonal velocities. There are however several important differences: In a horizontally unbounded flow with $\hat{v} = 0$ angular momentum around all points is conserved, so

$$\int_D \omega |r - r_0|^2 r\, dr\, d\phi \tag{5.1}$$

is conserved for *all* values of r_0. Thus, two vortices with the same sign are prevented from coming close together and merging at r_0 by an angular momentum barrier, unless (i) there is a third vortex to absorb the excess angular momentum, or (ii) the two vortices are initially both very close to each other (and to r_0), or (iii) the two vortices fragment and shed some ω during their merger, with the shed fragments moving far from r_0 carrying most of the angular momentum. If annular horizontal boundaries or a non-zero $\hat{v}$ are present, then angular momentum is conserved only about the origin; thus, two vortices initially far from each other have no angular momentum barrier and are free to come together and merge (but not at the origin). In fact, the differential rotation of $\hat{v}$ brings distant vortices close together on a fast, advective timescale. Another difference in which a zonal flow affects vortex mergers is that it allows an exchange between E^{self} and E^{int}. Small-scale filaments of ω dispersed throughout the zonal flow also cause a difference between the mergers of

vortices examined in this paper and the mergers of isolated vortices. These last two differences are important in the balance of energy and are discussed in detail in §5.3.

An example of a vortex merger in a zonal flow with uniform ω_p superposed with small-scale filaments of vorticity is shown in figure 10 (plates 7, 8). Initially (figure 10a) the zonal flow contains are no filaments – only two identical vortices positioned at the same radial location in the annulus and separated azimuthally by $55\pi/64$ rad. The initial stream function is

$$\psi(r, \phi) = -g(r, \phi - \tfrac{1}{2}\pi) - g(r, \phi + 41\pi/64), \tag{5.2}$$

where $g(r, \phi)$ is defined by (3.3). The bottom topography is $h(r) = (r - \tfrac{5}{6})$, and the zonal flow is $\hat{v}_\phi = \tfrac{1}{6}r(2r - R_{\mathrm{in}} - R_{\mathrm{out}})$, so that $\hat{\sigma}/\omega$ at the vortices is positive and of order unity. Our motivation for choosing the initial $55\pi/64$ rad separation is the following. A flow with two identical vortices initially separated by π rad is two-fold symmetric. Because the symmetry is preserved the vortices can never merge. However, the flow is linearly unstable to non-two-fold symmetric perturbations that move the two vortices to different radial locations. Once the two vortices are at different radial locations the differential rotation of $\hat{v}_\phi$ brings them together. Our numerical code is designed so that its round-off errors also preserve the two-fold symmetry. Thus our initial separation of $55\pi/64$ is used to break the symmetry while keeping the initial vortices well separated.

When the symmetry is removed, the v-component of the flow causes the two vortices to rotate about their common centre of vorticity; the vortex at $\phi = \pi$ moves quickly to a location with slightly larger radius, and the other to a smaller. Both vortices shed filaments and become more elliptical (figure 10b). The values of their ellipticities are related to the local value of $\hat{\sigma}/\omega$ as described in §3.7. Some filaments reattach to the large vortices, but about half do not and become distributed throughout the zonal flow with nearly uniform density. After the differential rotation in $\hat{v}_\phi$ brings the two vortices together (figure 10c), they merge and expel the less rotational, yellow and light-blue coloured fluid entrained between them (figure 10d). The close proximity of the two vortices just before merger produces a large strain which in turn causes two filamentary whiskers of ω to form (figure 10e, f). The whiskers break off (figure 10g) and fragment with some of the fragments rejoining the vortices, some going to the boundaries of the annulus and some distributing themselves throughout the zonal flow. Although the time for the vortices to approach each other is sensitive to the initial azimuthal separation, once the two vortices are separated by a vortex diameter, the merger itself takes between one and two turn-around times. Here, the characteristic turn-around time is defined to be $4\pi/0.34$. Note that the resulting merged vortex in figure 10 must have approximately the same strength of vorticity, total area, radial location, and ellipticity as the two initial vortices, owing respectively to the conservation of vorticity, circulation, angular momentum, and the fact that the ellipticity is a function of $\hat{\sigma}/\omega$. Dissipation and vortex shedding make the conservation laws inexact. For example, the area of the merged vortex in figure 10(h) inside the w = 0.25 contour is only 97% of the area in the initial flow in figure 10(a) for which $\omega \geqslant 0.25$. The missing 3% is mostly in the filaments distributed throughout the zonal flow. Less than 1% is lost by the numerical dissipation. The flow in figure 10(h) is time-dependent and is steady only in a statistical sense because ω is continually exchanged between the large vortex and the filaments in the zonal flow.

5.2. *Multiple mergers*

In order to determine whether or not all large vortices in a zonal flow merge together, we consider a zonal flow superposed initially with several large vortices all with approximately the same value of ω such that $\hat{\sigma}/\omega$ at the vortices is positive and of order unity. Our initial flow is the checkerboard pattern shown in figure 11(a) (plate 9). The initial distribution of ω is chosen to be slightly irregular (so that there are no symmetries that could be conserved by our initial-value code) and such that the vortices are square in shape (i.e. far from equilibrium so that they quickly shed some of their ω as filaments). The boundaries of the annulus, bottom topography, and $\hat{v}$ are the same as in figure 10. The initial vorticity in figure 11(a) is

$$\omega(r, \phi) = 0.56 \left(f(r, 0.58) \sum_{j=0}^{4} g\{\mathrm{mod}\,[(\phi - \tfrac{1}{2}\pi + \tfrac{2}{5}\pi j), 2\pi]\} \right.$$

$$+ f(r, 0.83) \sum_{j=0}^{5} g\{\mathrm{mod}\,[(\phi - \tfrac{1}{2}\pi + \tfrac{2}{6}\pi j), 2\pi]\}$$

$$\left. + f(r, 1.01) \sum_{j=0}^{7} g\{\mathrm{mod}\,[(\phi - \tfrac{1}{2}\pi + \tfrac{2}{8}\pi j), 2\pi]\} \right)$$

$$+ \omega_0, \tag{5.3}$$

where
$$f(r, s) \equiv \tfrac{1}{2}\{\tanh\,[30(r - s + 0.1)] - \tanh\,[30(r - s - 0.1)]\}, \tag{5.4}$$

$$g(\phi) \equiv \frac{1}{2}\left\{\tanh\left[\frac{128}{\pi}\left(\phi - \pi + \frac{\pi}{256}\right)\right] - \tanh\left[\frac{128}{\pi}\left(\phi - \pi - \frac{\pi}{256}\right)\right]\right\}, \tag{5.5}$$

and ω_0 is chosen to be consistent with the definitions of C_1 and C_2 in §2.2. The maximum value of the initial ω is 0.424. The 19 initial vortices shear, shed vorticity, approach each other, and merge (figure 11a–h) (plates 9, 10). The final flow has two elliptical vortices. The ellipticities of the two are different, but both are consistent with the ellipticity–$\hat{\sigma}/\omega$ relation discussed in §3.7. The vortex collisions cause a large amount of ω to be stripped from them. Although much of this ω gets dispersed throughout the zonal flow as filaments, approximately one-third is lost through dissipation; the flow in figure 11(h) has only 32% of the enstrophy of the initial flow value. The high rate of dissipation is because most of the stripped ω is put directly into the small, dissipative scales. Despite the large dissipation and stripping, the angular momentum is conserved to a few parts in 10^5, and the energy undergoes a reverse cascade. The energy spectra at three different times are shown in figure 12. Most of the energy of the non-axisymmetric component of the initial velocity is in azimuthal modes with $m > 5$. By 5.17 turn-around times, most shifts to the modes with $0 < m < 5$, and this reverse cascade continues for more than 58 turn-around times. An analysis of the enstrophy spectra show that enstrophy cascades to the small scales in bursts that correlate in time with the stripping of ω from the large vortices.

The fact that the final flow in figure 11(h) has two vortices is not significant. We have found examples of initial flows with 19 vortices that are only slightly different from the checkerboard arrangement in figure 11(a) that produce one, three, or four final vortices. The number of final vortices depends on the order in which the vortices merge. We have found that *two vortices merge if and only if their radial separation is less than a critical value which is of order the radius of the larger vortex.* (We calculate
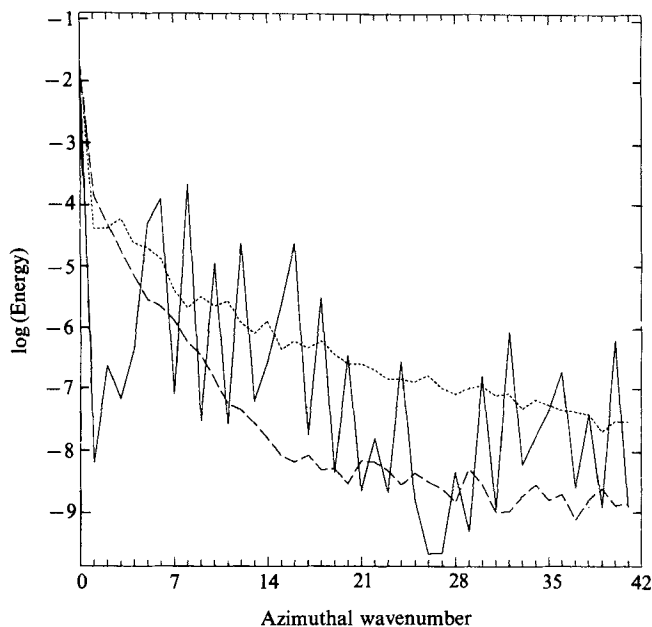
FIGURE 12. Energy spectra $\log_{10} E(m)$ of the flow in figure 11 with the solid curve after 0 turn-around times, dotted curve after 5.17, and long-dashed curve after 58.2.

this value in the next section.) Therefore when the vortices merge as in figure 11, so that the first mergers leave one cluster of vortices near the outer boundary and another near the inner, the vortices within each cluster merge into a single vortex. Because the two remaining vortices are then separated by more than a vortex radius they themselves do not merge together, and the final flow has two vortices. For the final flow to have only one vortex, it is necessary that the vortices merge in an order so that no vortex is ever cut off from its neighbours by a radial distance larger than a vortex radius.

Another interesting feature of multiple vortex mergers is the homogenization of potential vorticity in the final merged vortex. To demonstrate this we used the same initial checkerboard pattern as shown in figure 11 (*a*), but we gave each vortex a different and nearly constant value of ω ranging from $0.3\hat{\sigma}(r)$ to $3\hat{\sigma}(r)$. From the results in §4, we had expected that, in the limit of no numerical diffusion of vorticity, the distribution of ω within the final vortex would have arranged itself into distinctly stratified layers like an onion, with the largest ω at the vortex centre and decreasing monotonically outward. With numerical diffusion, we expected the boundaries between the layers to blur and the ω to decrease smoothly and monotonically from the vortex centre outward. Instead, we found that the final vortex had nearly uniform ω with a mean ω of $0.8\hat{\sigma}$ and a variation (in the central 75% of the vortex) less than 10%. Diffusion made approximately half the ω spin-up and half spin-down. The explanation for the unanticipated behaviour is the following. As the initial vortices merge they are broken into small fragments. Just after the fragments all bind together into a single vortex, there are two competing effects: (i) at a rate that increases with fragment size, the fragments stratify so that those with the largest $|\omega|$ are at the centre, and (ii) at a rate that decreases with fragment size, the vorticity of the fragments diffuses so it approaches a common value. In our numerical

experiments the size of the fragments and value of the numerical diffusion were such that the vorticity diffused to a constant value before the fragments had a chance to stratify.

In summary, we have found that vortices with $\hat{\sigma}/\omega > 0$ merge on a fast, advective timescale. Undoubtedly, this propensity to merge is responsible, at least in part, for the finite-amplitude stability of vortices with $\hat{\sigma}/\omega > 0$ in very turbulent shear flows like those studied by Sommeria *et al.* (1988). A vortex in a turbulent shear has fragments of ω continually torn from it. These fragments and other filaments in the zonal flow with $\hat{\sigma}/\omega > 0$ continually merge with the large vortex and a statistical equilibrium is maintained. If the zonal turbulence were to split the vortex into two, then the two pieces would recombine. Our numerical simulations show that vortices with $\hat{\sigma}(r)/\omega > 0$ merge with their neighbours (within a critical radial distance) and grow in area until all of the vortices have merged together, but there is one exception to this result: If the sign of $\hat{\sigma}(r)$ changes with r, then a vortex with $\hat{\sigma}(r)/\omega > 0$ merges and grows until part of it overflows into the region where the shear of the zonal flow changes sign. Van Buskirk & Marcus (1990) have shown that the vortex can only penetrate a finite distance into this region, and so the vortex continues to merge with other vortices of like sign, but the rate at which it gains area is balanced by the rate at which it loses it through the shedding of filaments in the region of the zonal flow where $\hat{\sigma}(r)/\omega < 0$.

5.3. *Critical separation distance for vortex merging*

In order to determine the critical separation for vortex merging, we ran a series of experiments consisting of a zonal flow superposed with two identical vortices whose centres were located radially at $r = \frac{1}{2}(R_{\mathrm{out}}+R_{\mathrm{in}}) \pm \frac{1}{2}\Delta r$ and separated azimuthally by $55\pi/64$ rad. By varying the impact parameter Δr and observing whether the two vortices merged, we determined the critical impact parameter Δr_{crit} above which vortices do not merge and below which they do. We carried out the experiments with two different zonal flows, one given by equation (3.1) and others by (3.9). We also varied the characteristic value of the initial vortices' ω from 0.3 to $3.0\hat{\sigma}\frac{1}{2}(R_{\mathrm{out}}+R_{\mathrm{in}})$ in increments of $0.2\hat{\sigma}\frac{1}{2}(R_{\mathrm{out}}+R_{\mathrm{in}})$. Each of the initial two vortices was designed so that it would have been in equilibrium if the other were not present and if it had been located at $r = \frac{1}{2}(R_{\mathrm{out}}+R_{\mathrm{in}})$. (We chose quasi-equilibria for initial conditions to help minimize the shedding of ω and thereby conserve the circulation of the large vortices.) Our initial flows also included the superposition of a uniform distribution of small-scale filaments of vorticity as described in §3.7.

To summarize our results: the two, initial, quasi-equilibrium vortices shed (without eventual reattaching) very little ω, less than 1% of their circulation. When two vortices merge, the angular momentum of the final vortex is within 1% of that of the two initial vortices. This implies that the transfer of angular momentum from the vortices to the filaments is nil. Less than 0.1% of the energy of the initial vortices is lost through dissipation, but there is a large transfer of energy, up to 10%, from the vortices to the filaments. When two vortices merge, the final vortex is always (statistically) steady with an ellipticity as described in §3.7. Using these observations we developed a test for predicting vortex merger based on energy arguments. The test successfully predicts the critical impact parameter Δr_{crit}.

To apply our test, first divide the velocity into two parts: (i) a large, temporally coherent component consisting of $\hat{v}$ and the component of v due to the large vortices, and (ii) a temporarlly incoherent part due to the filaments of ω in the zonal flow. (The coherent part is defined numerically by using a time-averaging algorithm.) If none

of the filaments of ω in the zonal flow merges with the vortices or attaches to the boundaries of the annulus, then the circulation and all of the enstrophies of both the temporally coherent and incoherent components are conserved independently. In addition, if the distribution of filaments remains macroscopically uniform throughout the zonal flow, the angular momenta of both components (which depend on the ω-weighted average value of r^2) are independently conserved. However, the energies of the two components are free to change. The energy of the temporally incoherent component changes when the microscopic distribution of filaments changes. For example, if pairs of like-signed filaments of ω bind together while keeping the macroscopic distribution of pairs uniform, the energy of the temporally incoherent component increases while keeping its circulation, enstrophy and momentum constant. Note that the total energy of the flow is the sum of three parts: the energy of the temporally coherent velocity, the energy of the temporally incoherent velocity, and the energy of the cross-term between these two components. However, if the macroscopic distribution of filaments remains uncorrelated with the vortices, then the value of the cross-term remains constant. Prior to running our initial-value simulations we do not know whether the two initial vortices will merge together. However, if we had *a priori* knowledge that they did merge, then we could determine in advance the velocity of the merged vortex flow without using our initial-value code. This is because we know the values of the circulations, enstrophies, and angular momenta of the merged vortex flow (assuming no filaments leave or join the incoherent component of the velocity), and we know that a merged vortex is steady. This information is sufficient to compute the coherent component of the final flow. As an analytic example, consider a plane-parallel, unbounded zonal flow with constant shear $\hat{\sigma}$, and let the two initial vortices have uniform ω with ellipticities given by the Moore–Saffman relation in figure 6. Then the final vortex (if one forms) is steady and has the same ω and ellipticity as the initial vortices and twice their area. By conservation of momentum, its location in the zonal flow is midway between the locations of the two initial vortices. Thus, the final flow with the single vortex is completely specified. Our numerical experiments with vortices of non-uniform ω in annular zonal flow with boundaries require a numerical calculation to compute the final flow, but the point is that it is uniquely determined by the conservation of the circulations, enstrophies, and angular momenta, but *not* energy. The energy of the coherent component of the final flow will in general not be equal to that of the initial flow. Therefore, the coherent and incoherent components must exchange energy for there to be mergers. Because we found empirically that the energy of the coherent component of the velocity decreases, our proposed test for vortex merger is this: calculate the energy of the coherent component of the velocity of the initial two-vortex flow and compare it with that of the one-vortex flow with the same circulations, enstrophies, and momenta; vortices merge if and only if the latter energy is smaller. This test agrees with the results of our numerical experiments. We can predict the value of Δr_{crit} to within 5%, where the uncertainty is due to our uncertainty in dividing the final flow into coherent and incoherent components (which depends on the timescale used in the averaging).

More importantly, we can determine semianalytically how Δr_{crit} depends qualitatively on $\hat{\sigma}$, ω, and the sizes of the initial vortices. To do this, note that the coherent component of the energy is itself a sum of two parts – the self-energy and the interaction energy. To determine how the interaction energy of the flow changes during a merger let us first consider the analytically tractable case of the merger of two identical Moore–Saffman vortices, each with ellipticity ϵ, area A, potential

vorticity ω_{e}, and minor radius R_{m} superposed on a zonal flow with constant shear $\hat{\sigma}$. From (2.20), the change in the interaction energy after merger is

$$\delta E_{\mathrm{c}}^{\mathrm{int}} = \frac{A^2 \hat{\sigma} \omega_{\mathrm{c}}}{4\pi\epsilon} \left[\left(\frac{\Delta r}{R_{\mathrm{m}}} \right)^2 - 1 \right] = \frac{A^2 \hat{\sigma} \omega_{\mathrm{c}}}{4\pi(1 + \hat{\sigma}/\omega_{\mathrm{c}}) f} \left[\left(\frac{\Delta r}{R_{\mathrm{m}}} \right)^2 - 1 \right], \tag{5.6}$$

where f is the slowly varying function of $\hat{\sigma}/\omega_{\mathrm{e}}$:

$$f(\hat{\sigma}/\omega_{\mathrm{c}}) \equiv \frac{1}{2}\left[1 + \left(1 + 4\frac{\hat{\sigma}}{\omega_{\mathrm{c}}} \Big/ \left(1 + \frac{\hat{\sigma}}{\omega_{\mathrm{c}}} \right)^2 \right)^{\frac{1}{2}} \right]. \tag{5.7}$$

We use the subscript c to denote the coherent component of any quantity. Equation (5.6) shows that for $\Delta r < R_{\mathrm{m}}$, the one-vortex flow has less interaction energy than the two-vortex flow when $\hat{\sigma}/\omega > 0$, and it has greater when $\hat{\sigma}/\omega < 0$, and vice versa for $\Delta r > R_{\mathrm{m}}$. When $\Delta r = R_{\mathrm{m}}$, merger does not change the interaction energy. For mergers in arbitrary, bounded, annular zonal flows, $\delta E_{\mathrm{c}}^{\mathrm{int}}$ must be calculated numerically, but it is qualitatively similar to equation (5.6). In particular, $\delta E_{\mathrm{c}}^{\mathrm{int}}$ depends only on the sign of $\hat{\sigma}/\omega_{\mathrm{c}}$ and not on the individual signs of $\hat{\sigma}$ and ω_{c}, and we find numerically that $\delta E_{\mathrm{c}}^{\mathrm{int}} = 0$ at a value of Δr approximately equal to the minor radius of one of the initial vortices. For example, for the zonal flow in equation (3.1)

$$\delta E_{\mathrm{c}}^{\mathrm{int}} = \frac{2A\hat{\sigma}}{3r} (\langle \omega_{\mathrm{c}}\, r^3 \rangle_2 - \langle \omega_{\mathrm{c}}\, r^3 \rangle_1), \tag{5.8}$$

where A is the area of one of the initial vortices, $\langle \omega_{\mathrm{c}}\, r^3 \rangle_i$ is the average value of $\omega_{\mathrm{c}}\, r^3$

$$\langle \omega_{\mathrm{c}}\, r^3 \rangle_i \equiv \frac{1}{A} \int \omega_{\mathrm{c}}\, r^3 r \, \mathrm{d}r \, \mathrm{d}\phi, \tag{5.9}$$

and the subscript i is 1 and 2 for the one- and two-vortex flows, respectively. The quantity $(\langle \omega_{\mathrm{c}}\, r^3 \rangle_2 - \langle \omega_{\mathrm{c}}\, r^3 \rangle_1)$ is negative when $\Delta r = 0$, increases monotonically with Δr, and passes through zero when $\Delta r \approx R_{\mathrm{m}}$, so (5.8) and (5.6) are qualitatively similar.

To determine how the self-energy of the coherent component of the velocity changes during merger, we parameterize it in terms of the dimensionless function ζ defined by

$$\delta E_{\mathrm{c}}^{\mathrm{self}} \equiv \frac{\zeta A^2 \omega_{\mathrm{c}}^2}{4\pi} \ln\left(\frac{D}{R_{\mathrm{m}}} \right), \tag{5.10}$$

where D is the distance between the two initial vortices. Generally, ζ cannot be computed in closed form, but it is of order unity and depends only on the geometry of the vortices; ζ is only a weak function of the zonal flow. When vortices merge, the distribution of ω_{c} becomes compact, so generically $\delta E_{\mathrm{c}}^{\mathrm{self}}$ is always positive regardless of the size of Δr or the signs of ω_{c} and $\hat{\sigma}$. (There are exceptions, for example when the final vortex is close to a boundary.) Our test for merger predicts that if two vortices approach each other, then they will merge if $\delta E_{\mathrm{c}}^{\mathrm{int}}$ is sufficiently negative that it overcomes the increase in $\delta E_{\mathrm{c}}^{\mathrm{self}}$. We define Δr_{crit} to be the value of impact parameter at which $\delta E_{\mathrm{c}}^{\mathrm{int}} + \delta E_{\mathrm{c}}^{\mathrm{self}} = 0$. For Moore–Saffman vortices

$$\frac{\Delta r_{\mathrm{crit}}}{R_{\mathrm{m}}} = \left[1 - \left(\frac{\omega_{\mathrm{c}}}{\hat{\sigma}} + 1 \right) \zeta f \ln\left(\frac{D}{R_{\mathrm{m}}} \right) \right]^{\frac{1}{2}}. \tag{5.11}$$

For $\Delta r < \Delta r_{crit}$ and $\hat{\sigma}/\omega > 0$, the coherent component of the energy decreases in a merger. Equation (5.11) shows that $\Delta r_{crit}/R_m$ is less than one and increases with the value of $\hat{\sigma}/\omega_c$ and with the value of R_m/D. We have found numerically that these relationships are also true for mergers in annular geometries with the zonal flows in (3.1) and (3.9).

5.4. *Vortices with $\hat{\sigma}/\omega < 0$*

Our assertion that vortex dynamics can often be predicted by assuming that the coherent component of the energy decreases can be tested by examining vortices in zonal flows with $\hat{\sigma}/\omega < 0$. Here, the fission of a vortex into two smaller vortices with a small Δr generically decreases the coherent component of the energy. With $\hat{\sigma}/\omega \leqslant -0.5$, our simulations show that an initial vortex stretches into a spiral and breaks into smaller and smaller fragments as in figure 1. When the initial vortices are large with $R_m \geqslant \frac{1}{4}(R_{out} - R_{in})$, the ω from the initial vortices ends up in one of three places: deposited in a boundary layer at R_{in} (which contributes a $1/r$ component to the coherent velocity), in a boundary layer at R_{out}, or in an approximately macroscopically uniform distribution of filaments that fills the entire annulus (which contributes a solid-body rotation component to the coherent velocity). Let the amount of circulation that ends up in each of the three regions be designated as Γ_{in}, Γ_{out}, and $\Gamma_{uniform}$, respectively. The values of each of the three circulations can be predicted by using (i) the assumption that the energy of the coherent component of the flow is minimized, (ii) the conservation of circulation Γ_c, and (iii) the conservation of the angular momentum L_c. (Note that because the initial vortices fragment into pieces that become part of the incoherent component, the enstrophies of the coherent component are not conserved). With the zonal flow of equation (3.1), the conservation of circulation and momentum and the minimization of the coherent energy yield the following:

$$\Gamma_{in} = \frac{4 L_c R_{in}^2}{R_{out}^4 - R_{in}^4} - \eta, \tag{5.12}$$

$$\Gamma_{uniform} = \frac{4 L_c}{R_{out}^2 + R_{in}^2} + 2\eta \tag{5.13}$$

and

$$\Gamma_{out} = \Gamma_{in} + \Gamma_c - \frac{4 L_c}{R_{out}^2 - R_{in}^2}, \tag{5.14}$$

where

$$\eta \equiv -\frac{2\pi}{45} \frac{5(R_{out}^3 - R_{in}^3) - 4\dfrac{R_{out}^5 - R_{in}^5}{R_{out}^2 - R_{in}^2}}{\left(\dfrac{R_{out}^2 + R_{in}^2}{R_{out}^2 - R_{in}^2}\right)\left[\left(\dfrac{R_{out}^2 + R_{in}^2}{R_{out}^2 - R_{in}^2}\right)\ln\dfrac{R_{out}}{R_{in}} - 1\right]}. \tag{5.15}$$

There is a physical additional constraint: Γ_{in}, Γ_{out}, and $\Gamma_{uniform}$ must all have the same sign as the ω of the original vortex. If either Γ_{in} or Γ_{out} have the opposite sign as ω, (5.12) is replaced with

$$\Gamma_{in} = \begin{cases} 0 & \text{if} \quad |\Gamma_c(R_{out}^2 - R_{in}^2)| > 4|L_c| \\ 4\dfrac{L_c}{R_{out}^2 - R_{in}^2} - \Gamma_c & \text{if} \quad |\Gamma_c(R_{out}^2 - R_{in}^2)| \leqslant 4|L_c|. \end{cases} \tag{5.16}$$

and $\Gamma_{uniform}$ and Γ_{out} are still given by (5.13) and (5.14). (Note that $\Gamma_{uniform}$ always has the same sign as ω for $R_{out}/R_{in} = 4$.) The results of our numerical simulations agree

with these predictions to within 15 %, although we note that when initial flows have small vortices with $R_m < \frac{1}{10}(R_{out} - R_{in})$, the fragments are not uniformly mixed in the zonal flow (they retain the memory of their initial radial location), and the final values of Γ_{in} can deviate significantly from the predicted values.

Our test for vortex mergers was based on the assumption that the timescale for merger is faster than the dissipative timescale. It also assumed that the timescales for vortices to shed or absorb small filaments and for changes in the macroscopic distribution of filaments are slow, so that the circulations, enstrophies, and angular momenta of the coherent component of the flow are conserved during merger. Our test further assumed that the filaments irreversibly absorb energy from the coherent component. Although it is intriguing how well the assumptions hold for mergers and for predicting the strengths of boundary layers, they do not always hold, and the general behaviour of vortices cannot always be predicted with them (see §6).

We conclude this section by emphasizing that there are qualitative differences between the flows studied here and those without small-scale filaments (or some other relaxation mechanism). In non-dissipative flows without filaments, there is in general no steady one-vortex flow that has the same circulation, enstrophies, momenta, and energy as an arbitrary initial flow that contains two vortices. Therefore it is impossible for the two initial vortices to merge into a steady flow with one vortex. The small filaments of ω in our simulations allow the large coherent vortices to reduce their energy so that the flow can make a transition from one steady state to another. The role played by the filaments is not the same as viscosity. In viscous flows the enstrophies and energy decrease monotonically, and the angular momentum decreases or increases; whereas in flows with small-scale filaments of ω (that obey the assumptions of this section) only the energy of the coherent component decreases while all of the other quantities remain constant. In weakly dissipative flows (with no zonal components, no boundaries, and no distribution of small filaments of ω) Dritschel (1985) argued that a two-vortex flow evolves to a one-vortex final state if the initial and final flows have the same momenta and circulations and if the change in energy between the initial and final states has the smallest value of all possible final states. Using this argument he was able to explain why his merging vortices always passed through a long-lived transient state with the same approximate ellipticity. However, starting with the long-lived state, he was unable to predict the direction of the flow evolution, i.e. whether the state evolves to a one- or a two-vortex flow. Our simulations show that these arguments do not carry over to flows with small-scale filaments of vorticity. Moreover in our simulations with filaments of ω, the assumption that the energy flows from the coherent to the incoherent component always gives an unambiguous direction to the flow's evolution, and so always predicts the direction in which a transient evolves.

6. Discussion
6.1. Summary of numerical results

We have shown how large vortices merge, migrate, fragment, and stretch in a shearing zonal flow in which there are also small-scale filaments of vorticity. The zonal flow breaks the degeneracy of the clockwise and counterclockwise vortices by allowing an exchange between the self-energy of the vortices and the interactions energy of the zonal flow. The small-scale filaments of vorticity allow the large-scale vortices to relax to equilibrium by absorbing their energy while conserving their

circulations and angular momenta. The decomposition of the flow into a zonal component with uniform potential vorticity and a remainder vorticity ω is useful because the zonal flow advects and stretches ω, but ω does not react back upon the zonal flow. The statistically steady vortices in an annular shearing zonal flow that we found numerically are similar to the Moore–Saffman vortices of piecewise-constant ω embedded in an unbounded, plane-parallel, zonal flow with uniform shear. We showed that a vortex with $4 > \hat{\sigma}/\omega > 0$ is robust, whereas a vortex with $-0.2 \leqslant \hat{\sigma}/\omega < 0$ is unstable to a finite-amplitude perturbation, and we numerically found that the lengthscale of the finite-amplitude perturbation is approximately equal to the distance between the boundary of the vortex and its last closed streamline. Initial vortices with $\hat{\sigma}/\omega < -0.2$ are not in equilibrium nor is there a nearby equilibrium to which they can evolve. Instead, they are pulled by the zonal flow into spirals and their ω is pushed outward to the radial extremities of the zonal flow. If the ω is pushed into a region where the shear of the zonal flow changes sign, then the ω rolls up into a stable vortex. We have shown that stable vortices are advected with a speed that is equal to the sum of the velocity of the surrounding zonal flow and the velocity due to the neighbouring vortices and boundaries (as determined by the Biot–Savart law). The breakup of a vortex layer demonstrates the exchange of energy between the self-energy and the interaction energy. Unstable layers with $\hat{\sigma}/\omega < 0$ are shown (analytically) at early times and (numerically) at late times to decrease their self-energy, which is consistent with the observation that these layers break into successively smaller filaments. Unstable layers with $\hat{\sigma}/\omega > 0$ are shown to increase their self-energy, which is consistent with the observation that these layers form a single large vortex. When large vortices are created by the binding together of smaller vortices, the ω of the smaller fragments redistributes itself, and there are two competing effects. One is that the ω within each fragment diffuses so that the ω throughout the entire vortex evolves towards a mean value on a timescale that increases with fragment size; this was observed in the mergers in §5. The other effect is that the fragments themselves move so that there is not a local minimum of $|\omega|$ in the vortex interior. The timescale of this effect decreases with fragment size; this was demonstrated in §4. In a series of experiments that began with two vortices separated radially by a distance Δr we showed that there existed a critical value Δr_{crit} above which vortices do not merge and below which they do. A theoretical value of Δr_{crit} was calculated by assuming that energy flows irreversibly from the two large vortices to the small filaments of ω. The theory was confirmed by the numerical experiments to within 5%.

6.2. *Future work*

A number of questions about the behaviour of vortices in the presence of zonal flows with small-scale filaments of ω have been raised by this study. For example, we have demonstrated that there are at least two cases in which the filaments absorb energy from the large scales, but this does not happen in all flows. In particular, in laboratory flows (Sommeria *et al.*), the Jovian atmosphere, and in some of our unpublished numerical experiments, vortices drift across zonal flows to locations where the zonal shear has a local maximum. It is easily shown that these locations correspond to local maxima of the coherent component of the energy which implies that energy flows from the filaments to the large vortices. This effect needs to be examined in detail. It suggests to us a model of vortex dynamics in which the large vortices are in a thermal bath of filaments – if the filaments are 'cool', then energy

flows from the large vortices to the filaments, and if they are 'warm', vice versa. Currently, we are carrying out several numerical experiments to test these ideas and in particular how vortices and filaments come to equilibrium. Another question raised by this study is under what conditions the potential vorticity becomes approximately uniform over large regions. In this paper we have shown that when large vortices are created in a weakly diffusive flow by the mergers of small fragments, their cores have nearly uniform ω_p. In the laboratory, Sommeria *et al.* showed that large zonal flows with nearly uniform ω_p are created by external forcing. However, a careful numerical study of flows with physically realistic forcing and dissipation will be needed to understand better the homogenization of ω_p.

Perhaps the best laboratories for studying the interactions of large vortices with zonal flows are the atmospheres of Jupiter, Saturn, and Neptune. It was the observations of long-lived Jovian vortices that initially motivated this paper. A brief study of the dynamics of the Jovian Great Red Spot was reported earlier (Marcus 1988), and detailed comparisons between the Jovian velocities and numerical simulations are quite good when the vertical structure of the atmosphere is taken into account (i.e. using the quasi-geostrophic equations with a finite value of the Rossby deformation radius in the definition of ω_p in equation (2.2) – see Marcus & Van Buskirk 1990). We conclude this section by listing the properties of the Red Spot that are shared by the vortices examined in this paper (and the vortices computed with the quasi-geostrophic equation with finite Rossby deformation radius). the *Voyager* satellite observations of the Red Spot show that it is a nearly two-dimensional vortex embedded in a zonal flow with a shear approximately equal to the vorticity of the Red Spot. The core of the Red Spot has nearly uniform potential vorticity (Dowling & Ingersoll 1989; Marcus & Van Buskirk 1990) which is consistent with a picture that it is slightly diffusive and was created by the merger of many small vortices. The Red Spot has the same sense of rotation as the local zonal shear, which is consistent with our numerical results that show that vortices with $0 < \hat{\sigma}/\omega = O(1)$ are robust. In fact, there are no observations of long-lived Jovian vortices with $\hat{\sigma}/\omega < 0$. The elliptical shape of the Red Spot is consistent with the shape of a vortex with uniform potential vorticity embedded in a zonal flow with $\hat{\sigma}/\omega_p = O(1)$. The Red Spot and the other long-lived Jovian vortices move around the planet at a speed equal to the velocity of the local zonal flow (to within the observational uncertainties). The Red Spot continually merges with and swallows nearby vortices of like sign but, similar to the vortices discussed at the end of §5.2, its growth is checked by the fact that it not only completely fills the local band of zonal flow where $\hat{\sigma}/\omega > 0$ but also spills over into the neighbouring region of zonal flow where $\hat{\sigma}/\omega < 0$.

Appendix. Vortex layer stability

A.1. *Eigenmodes*

The flow consisting of the zonal velocity $\hat{v}_\phi$ superposed on a vortex layer with piecewise-constant vorticity equal to ω in the strip $\bar{R}_1 \leqslant r \leqslant \bar{R}_2$ and vorticity equal to zero outside the strip has linear eigenmodes of the form $e^{im(\phi - ct)}$ where

$$c = \left(\frac{u_\phi(\bar{R}_2)}{2\bar{R}_2} + \frac{u_\phi(\bar{R}_1)}{2\bar{R}_1}\right) \pm \frac{|\omega|}{2m} \left\{\left[m\left(\frac{1-\gamma^2}{2}\right)\left(\frac{\langle \hat{\sigma}\rangle + \omega}{\omega}\right) - 1\right]^2 - \gamma^{2m}\right\}^{\frac{1}{2}}, \qquad (A\ 1)$$

where m is a positive integer, and where γ and $\langle \hat{\sigma}\rangle$ are defined in §4. The mth mode is linearly unstable if and only if

$$\frac{1}{m}(1 - \gamma^m) < \left(\frac{1-\gamma^2}{2}\right)\left(\frac{\langle \hat{\sigma}\rangle + \omega}{\omega}\right) < \frac{1}{m}(1 + \gamma^m). \qquad (A\ 2)$$

Clearly the flow is stable to all modes if $\langle \hat{\sigma}\rangle / \omega \leqslant -1$. The fastest growing eigenmode is given by (4.5).

In the limit of a thin vortex layer, or $\gamma \to 1$, the annular vortex layer has the same stability properties as a planar vortex layer with vorticity equal to ω for $\bar{Y}_1 \leqslant y \leqslant \bar{Y}_2$ and vorticity zero outside this strip. The eigenmodes of the planar vortex layer are of the form $e^{i\alpha(x - ct)/(\bar{Y}_2 - \bar{Y}_1)}$, and the planar vortex layer is unstable if and only if

$$\left[\alpha \frac{\langle \hat{\sigma}\rangle + \omega}{\omega} - 1\right]^2 - e^{-2\alpha} < 0 \qquad (A\ 3)$$

for some positive wavenumber α. For the planar vortex layer in (A 3) we have defined

$$\langle \hat{\sigma}\rangle \equiv [\hat{v}_x(\bar{Y}_1) - \hat{v}_x(\bar{Y}_2)]/(\bar{Y}_2 - \bar{Y}_1). \qquad (A\ 4)$$

For thin layers, i.e. $(\bar{Y}_2 - \bar{Y}_1) \to 0$, $\langle \hat{\sigma}\rangle$ approaches the value of $\hat{\sigma}$ at the layer. In the thin-layer limit, (A 2) and (A 3) are the same if one identifies the planar wavenumber α with $\frac{1}{2}m(1 - \gamma^2)$ and uses the fact that in the thin limit, γ^{2m} approaches $e^{-2\alpha}$. The stability limits and fastest growing eigenmode as a function of α and $(\langle \hat{\sigma}\rangle + \omega)/\omega$ are shown in figure 9. The unstable linear eigenmode changes the location of the edges of the vortex layer from $\bar{Y}_1$ to $\bar{Y}_1 + \delta_1 e^{i\alpha(x - ct)/(\bar{Y}_2 - \bar{Y}_1)}$ and from $\bar{Y}_2$ to $\bar{Y}_2 + \delta_2 e^{i\alpha(x - ct)/(\bar{Y}_2 - \bar{Y}_1)}$. For unstable eigenmodes

$$\frac{\delta_1}{\delta_2} = -e^{\alpha}\left\{\frac{i\omega}{|\omega|}\left[e^{-2\alpha} - \left(\alpha \frac{\langle \hat{\sigma}\rangle + \omega}{\omega} - 1\right)^2\right]^{\frac{1}{2}} + \alpha \frac{\langle \hat{\sigma}\rangle + \omega}{\omega} - 1\right\}. \qquad (A\ 5)$$

Equation (A 5) shows that $|\delta_1/\delta_2| \equiv 1$, so the perturbation's amplitudes at the two edges of the layer are equal regardless of the value of $\hat{v}_x(y)$. The perturbations of the annular vortex layer do not have equal amplitudes at the two edges except in the limit $\gamma \to 1$.

The stability analysis of a piecewise-constant vortex layer in a zonal flow is a special case of the analysis of a zonal flow superposed on a vortex with $\omega = \omega_1$ for $r \leqslant \bar{R}_1$, with $\omega = \omega_2$ for $\bar{R}_1 < r \leqslant \bar{R}_2$ and $\omega = 0$ for $r > \bar{R}_2$. This vortex (referred to in §4) is unstable if and only if

$$\left[m\left(\frac{1-\gamma^2}{2}\right)\left(\frac{\langle \hat{\sigma}\rangle + \omega_2 - \omega_1}{\omega_2}\right) - 1 + \frac{\omega_1}{2\omega_2}\right]^2 - \gamma^{2m}\left(1 - \frac{\omega_1}{\omega_2}\right) < 0 \qquad (A\ 6)$$

for some positive integer m where $\langle \hat{\sigma} \rangle$ is defined by (4.6). A vortex with $\omega_1/\omega_2 < 1$ and $(\langle \hat{\sigma} \rangle + \omega_2 - \omega_1)/\omega_2 > 0$ is, in general, unstable. In particular, the vortex is unstable to the eigenmode with wavenumber

$$m = \left(1 - \frac{\omega_1}{2\omega_2}\right)\left(\frac{\omega_2}{\langle \hat{\sigma} \rangle + \omega_2 - \omega_1}\right)\left(\frac{2}{1 - \gamma^2}\right). \tag{A 7}$$

Though the m defined by (A 7) is positive for the constraints mentioned above, it may not be an integer and therefore physically allowable. Generally, the integers closest to this m make the left-hand side of (A 6) negative and the vortex unstable. However, for some very small values of γ, the left-hand side of (A 6) is positive for all positive integers m, and the vortex is linearly stable.

A.2. *Stabilization of vortex layers with* $\langle \hat{\sigma} \rangle/\omega < -1$

The above analysis shows that an annular or planar vortex layer is linearly stable if $\langle \hat{\sigma} \rangle/\omega \leqslant -1$, and it is worthwhile to show both mathematically and physically how a zonal flow with $\langle \hat{\sigma} \rangle$ opposite in sign to and greater in magnitude than ω stabilizes the layer. Fjortoft's theorem and the inflection theorem can be used to determine linear stability. The inflection theorem is: In an annular geometry with arbitrary $h(r)$ and $\hat{v}_\phi(r)$, a necessary condition for linear instability (in the form of discrete spectrum eigenmodes) of an axisymmetric azimuthal flow $u_\phi(r) \equiv \hat{v}_\phi(r) + v_\phi(r)$ is that ω has an extremum somewhere in the flow's interior not including the radial boundaries. Fjortofts's theorem is: If the extremum occurs at r_e, then to be unstable there must be at least one point in the flow where $[u_\phi(r)/r - u_\phi(r_e)/r_e]\partial\omega/\partial r < 0$. (NB Rayleigh's test for centrifugal instability – linear instability is equivalent to the radial decrease of the absolute value of the angular momentum per unit mass – is not valid for two-dimensional flows.) To see mathematically how a zonal flow with $\hat{\sigma}/\omega < -1$ stabilizes a vortex layer, consider an axisymmetric vortex layer in which ω is continuous, differentiable, positive, and has a single maximum at r_e such that $R_{\rm in} < r_e < R_{\rm out}$. In addition let $v_\phi(R_{\rm in}) \geqslant 0$. If $\hat{v}_\phi \equiv 0$, then the flow could be either stable or unstable depending upon the exact form of $\omega(r)$. However, if $\hat{v}_\phi \neq 0$, we claim that a sufficient condition for linear stability is that

$$\hat{\sigma}(r)/\omega(r) < -1 \tag{A 8}$$

for all $R_{\rm in} < r < R_{\rm out}$. To prove this statement, we need to show that

$$[u_\phi(r)/r - u_\phi(r_e)/r_e]\frac{\partial\omega}{\partial r} > 0$$

for all r. By assumption there is a single maximum in ω, so $\partial\omega/\partial r > 0$ for $r < r_e$, and $\partial\omega/\partial r < 0$ for $r > r_e$. Therefore a sufficient condition for linear stability is that $\partial(u_\phi/r)/\partial r < 0$ for all r, or equivalently $\hat{\sigma} + \omega - 2v_\phi/r < 0$, or equivalently

$$\hat{\sigma}/\omega < -1 + 2v_\phi/\omega r \tag{A 9}$$

for all r. However

$$v_\phi(r) = v_\phi(R_{\rm in})\frac{R_{\rm in}}{r} + \frac{1}{r}\int_{R_{\rm in}}^{r} \omega r \, {\rm d}r,$$

so if $v_\phi(R_\phi) \geqslant 0$, then $v_\phi(r) > 0$ for all r. Therefore condition (A 8) sufficiently satisfies (A 9). Clearly, the stability condition of (A 8) applies also to vortex layers with $\omega < 0$ and with a single minimum in ω.

To obtain a more physical understanding of how the zonal flow stabilizes a vortex layer, we note that in the thin-layer limit an annular vortex layer has the same stability properties as a thin planar vortex layer, which in turn has the same properties as a planar vortex sheet. The vortex sheet in turn has the same stability properties of a row of discrete vortices. Therefore we shall demonstrate the physical mechanism by which a shearing zonal flow stabilizes a vortex layer by examining how it affects a row of vortices. However, we must first relate the stability of a vortex sheet to a vortex layer. Consider a vortex sheet with a jump in the velocity across the sheet equal to Δv. Define $\langle \hat{\sigma} \rangle$ to be the shear of the zonal flow at the location of the sheet, and let $\langle \omega \rangle \equiv -\frac{1}{2}\alpha\Delta v$, where α is the wavenumber of the perturbation of the sheet. Although the vorticity of the sheet is singular $\langle \omega \rangle$ is well-defined, has the same dimensional units, and plays a role in the linear dynamics of a vortex sheet that is analogous to the role ω plays in the vortex layer. In particular, it is trivial to show that the sheet is stable to linear perturbations with wavenumber α when $\langle \hat{\sigma} \rangle / \langle \omega \rangle < -1$. Now model the vortex sheet with a row of discrete potential vortices (Lamb 1932), each with circulation $-\lambda\Delta v$, and each equally spaced a distance λ apart as shown in figure 13(a). To see that this row of vortices has the same long-wavelength (i.e. wavelength greater than λ) instabilities as the vortex sheet, observe that the coordinates of the jth vortex obey

$$\frac{\mathrm{d}y_j}{\mathrm{d}t} = -\frac{\lambda\Delta v}{2\pi} \sum_{m \neq j} \frac{x_j - x_m}{(x_j - x_m)^2 + (y_j - y_m)^2}, \tag{A 10}$$

$$\frac{\mathrm{d}x_j}{\mathrm{d}t} = \hat{v}_x(y_j) + \frac{\Delta v}{2} + \frac{\lambda\Delta v}{2\pi} \sum_{m \neq j} \frac{y_j - y_m}{(x_j - x_m)^2 + (y_j - y_m)^2}. \tag{A 11}$$

Equations (A 10) and (A 11) have linear eigenmodes

$$y_j = \mathrm{e}^{\mathrm{i}\alpha(j\lambda - ct)}, \tag{A 12}$$

$$x_j = \mp\left(1 + \frac{\langle \hat{\sigma} \rangle}{\langle \omega \rangle}\right)^{\frac{1}{2}} \mathrm{e}^{\mathrm{i}\alpha(j\lambda - ct)}, \tag{A 13}$$

where $\langle \hat{\sigma} \rangle$ is the shear of the zonal flow at the row of vortices, and now $\langle \omega \rangle$ is defined as

$$\langle \omega \rangle \equiv -\frac{\Delta v}{2}\alpha\left(1 - \frac{\alpha\lambda}{2\pi}\right) \tag{A 14}$$

(with the restriction that $2\pi/\lambda > \alpha > 0$), and where $j\lambda$ acts like the x-coordinate in the vortex sheet. The eigenvalues are (NB the signs in (A 13))

$$c = \hat{v}_x + \frac{\Delta v}{2} \pm \mathrm{i}\frac{\Delta v}{2}\left(1 + \frac{\langle \hat{\sigma} \rangle}{\langle \omega \rangle}\right)^{\frac{1}{2}}\left(1 - \frac{\alpha\lambda}{2\pi}\right), \tag{A 15}$$

where $\hat{v}_x$ is the zonal velocity at the row of vortices. In the limit that $1/\alpha$ is much greater than λ, the definitions of $\langle \omega \rangle$, the dispersion relations, and the conditions for linear stability are the same for the row of discrete potential vortices and the vortex sheet. We therefore argue that the dynamics of a row of discrete vortices, a vortex sheet, and a vortex layer are all controlled by the same physics. To understand this physics consider the rows of potential vortices in figure 13. Let the potential vortices all have the same strength and sign (in this case positive), so $\Delta v < 0$. Figure 13 is in the frame of reference of an observer moving with velocity $\hat{v}_x + \frac{1}{2}\Delta v$. Now perturb
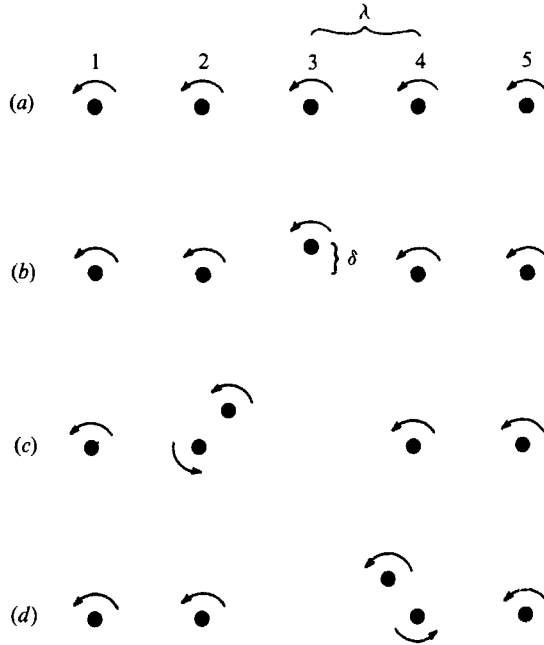
FIGURE 13. Sketch showing the instabilities of a row of vortices separated from each other by a distance λ (a). The third vortex is displaced upward a distance δ (b). If $\hat{\sigma}$ is zero or has the same sign as the vortices in the sheet, vortex 3 is advected to the left, and its nearest neighbour, vortex 2, will push it upward further away from the original location of the vortex sheet. The flow is unstable (c). If $\hat{\sigma}$ is opposite in sign to and greater in magnitude than the vortices in the sheet, vortex 3 is pushed to the right. Vortex 4 becomes the nearest neighbour and pushes vortex 3 downward back into the sheet. The flow is stable (d).

vortex number 3 upward a distance δ. If this vortex is forced downwards back into the sheet the flow is stable, and if it is advected further upward it is unstable. Vortex 3 is always advected to the left by the other vortices in the sheet. It is advected either to the left or the right by $\hat{v}$ depending on the sign of $\langle\hat{\sigma}\rangle$. Vortex 3 is not advected initially in the y-direction. If vortex 3 were advected to the left it would interact most strongly with vortex 2 which pushes it upward away from the sheet (figure 13c). Therefore advection to the left is equivalent to unstable flow. If vortex 3 were advected to the right, then vortex 4 would push it downward back into the sheet the flow would be stable. If $\langle\hat{\sigma}\rangle$ is positive, then both the advection due to the row of vortices and due to $\hat{v}$ push vortex 3 to the left, and the flow is unstable (figure 13c). If $\langle\hat{\sigma}\rangle$ at the sheet is negative, then $\hat{v}$ pushes vortex 3 to the right with velocity $|\langle\hat{\sigma}\rangle|\delta$ (to first order in δ). The velocity exerted on vortex 3 due to the row is well-approximated by the velocity due to just the two nearest neighbours, vortices numbers 2 and 4. To first order in δ, this velocity is to the left and has magnitude $|\delta\Delta v/\pi\lambda|$. Therefore if

$$\frac{\langle\hat{\sigma}\rangle}{\langle\omega\rangle} < -\frac{2}{\pi\alpha\lambda(1-\alpha\lambda/2\pi)} \tag{A 16}$$

then vortex 3 moves to the right, and the flow is stable. The stability condition given by (A 16) only approximates the stability condition given by (A 8) because we have limited our analysis to nearest neighbours. However, the key point of our physical analysis is that *instability (or stability) is equivalent to vortex 3 being advected to the left*

(*or right*). This point is not a consequence of the fact that we used only the influence of the nearest neighbours in determining the motion of vortex 3; indeed, it is verified by the analysis of the linear perturbations of the infinite row of potential vortices: At time $t = 0^+$, let all of the vortices in the row be perturbed from their equilibrium positions by a linear eigenmode, and choose its phase and amplitude such that vortex 3 is displaced upward a distance δ but is not displaced to the left or right. Then if $\langle\hat{\sigma}\rangle/\langle\omega\rangle \leqslant -1$, so that the flow is stable, the position of vortex 3 at later times is (when viewed in a frame moving with velocity $\hat{v}_x + \frac{1}{2}\Delta v$)

$$x_3(t) = |\delta|\left(-1 - \frac{\langle\hat{\sigma}\rangle}{\langle\omega\rangle}\right)^{\frac{1}{2}} \sin\left[\alpha|\Delta v|\left(1 - \frac{\alpha\lambda}{2\pi}\right)\left(-1 - \frac{\langle\hat{\sigma}\rangle}{\langle\omega\rangle}\right)^{\frac{1}{2}}\tfrac{1}{2}t\right] + x_3(0), \qquad \text{(A 17)}$$

$$y_3(t) = |\delta|\cos\left[\alpha|\Delta v|\left(1 - \frac{\alpha\lambda}{2\pi}\right)\left(-1 - \frac{\langle\hat{\sigma}\rangle}{\langle\omega\rangle}\right)^{\frac{1}{2}}\tfrac{1}{2}t\right] + y_3(0). \qquad \text{(A 18)}$$

If $\langle\hat{\sigma}\rangle/\langle\omega\rangle > -1$, so that the row is unstable, then

$$x_3(t) = -|\delta|\left(1 + \frac{\langle\hat{\sigma}\rangle}{\langle\omega\rangle}\right)^{\frac{1}{2}} \sinh\left[\alpha|\Delta v|\left(1 - \frac{\alpha\lambda}{2\pi}\right)\left(1 + \frac{\langle\hat{\sigma}\rangle}{\langle\omega\rangle}\right)^{\frac{1}{2}}\tfrac{1}{2}t\right] + x_3(0), \qquad \text{(A 19)}$$

$$y_3(t) = |\delta|\cosh\left[\alpha|\Delta v|\left(1 - \frac{\alpha\lambda}{2\pi}\right)\left(1 + \frac{\langle\hat{\sigma}\rangle}{\langle\omega\rangle}\right)^{\frac{1}{2}}\tfrac{1}{2}t\right] + y_3(0). \qquad \text{(A 20)}$$

These eigenmode solutions show that in a stable row of vortices, vortex 3 is advected initially to the right, and in an unstable row initially to the left. This verifies the key point of the nearest-neighbour analysis, and it shows that for $\hat{v}_\phi$ to stabilize a vortex layer it must overcome the circulation of the vortex layer and advect the perturbations of the sheet or layer in the direction opposite to the circulation.

REFERENCES

BENZI, R., PATARNELLO, S. & SANTNGELO, P. 1987 On the statistical properties of two-dimensional decaying turbulence. *Europhys. Lett.* **3**, 811–818.

BUTTKE, T. F. 1990 The observation of singularities in the boundary of patches of constant vorticity. *Phys. Fluids* (to appear).

DOWLING, T. E. & INGERSOLL, A. P. 1989 Jupiter's Great Red Spot as a shallow-water system. *J. Atmos. Sci.* **46**, 3256–3278.

DRITSCHEL, D. G. 1985 The stability and energetics of corotating uniform vortices. *J. Fluid Mech.* **157**, 95–134.

FLIERL, G. R., STERN, M. E. & WHITEHEAD, J. A. 1983 The physical significance of modons. Laboratory experiments and general integral constraints. *Dyn. Atmos. Oceans* **7**, 233–263.

LAMB, H. 1932 *Hydrodynamics*. Cambridge University Press.

MARCUS, P. S. 1984a Simulation of Taylor–Couette flow. Part 1. Numerical methods and comparison with experiment. *J. Fluid Mech.* **146**, 45–64.

MARCUS, P. S. 1984b Simulation of Taylor–Couette flow. Part 2. Numerical results for wavy-vortex flow with one travelling wave. *J. Fluid Mech.* **146**, 65–113.

MARCUS, P. S. 1986 Numerical simulations of quasi-geostrophic flow using vortex and spectral methods. In *Numerical Analysis* (ed. D. F. Griffiths & G. A. Watson), pp. 125–139. Longman.

MARCUS, P. S. 1987 Spatial self-organization of vortices in chaotic shearing flows. *Nucl. Phys.* B (*Proc. Suppl.*) **2**, 127–138.

MARCUS, P. S. 1988 Numerical simulations of Jupiter's Great Red Spot. *Nature* **331**, 693–696.

MARCUS, P. S. & VAN BUSKIRK, R. 1990 Comment on 'Jupiter's Red Spot as a shallow-water system'. *J. Atmos. Sci.* (to appear).

MAXWORTHY, T. & REDEKOPP, L. G. 1976 A solitary wave theory of the Great Red Spot and other observed features in the Jovian atmosphere. *Icarus* **29**, 261–271.

MELANDER, M. V., STYCZEK, A. S. & ZABUSKY, N. J. 1984 Elliptically desingularized vortex model for the two-dimensional Euler equations. *Phys. Rev. Lett.* **53**, 1222–1225.

MOORE, D. W. & SAFFMAN, P. G. 1971 Structure of a line vortex in an imposed strain. In *Aircraft Wake Turbulence* (ed. J. H. Olsen, A. Goldburg & M. Rogers), pp. 339–354. Plenum.

NIELSEN, J. E. & SCHOBERL, M. R. 1984 A numerical simulation of barotropic instability. Part II: Wave–wave interaction. *J. Atmos. Sci.* **41**, 2869–2881.

ORSZAG, S. A. 1974 Fourier series on spheres. *Mon. Weath. Rev.* **102**, 56–75.

OVERMAN, E. A. & ZABUSKY, N. J. 1982 Evolution and merger of isolated vortex structures. *Phys. Fluids* **25**, 1297–1305.

RHINES, P. B. & YOUNG, W. R. 1982 Homogenization of potential vorticity in planetary gyres. *J. Fluid Mech.* **122**, 347–367.

SOMMERIA, J., MEYERS, S. D. & SWINNEY, H. L. 1988 Laboratory simulation of Jupiter's Great Red Spot. *Nature* **331**, 689–693.

VAN BUSKIRK, R. D. & MARCUS, P. S. 1990 Contour methods for vortices in shearing zonal flows. *Bull. Am. Phys. Soc.*